The Effect of Fluoride on the Structure, Function, and Proteome of Intestinal Epithelia

Flávia Amadeu de Oliveira,[1,2] Lesley J MacVinish,[1] Simran Amin,[1] Duleni Herath,[1] Pia Jeggle,[1] Ioanna Mela,[1] Maria Pieri,[1] Chetanya Sharma,[1] Gavin E Jarvis,[3] Flávia M Levy,[2] Mariana R Santesso,[2] Zohaib N Khan,[2] Aline L Leite,[2] Rodrigo C Oliveira,[2] Marília AR Buzalaf,[2] J Michael Edwardson[1]

[1]Department of Pharmacology, University of Cambridge, Cambridge, UK

[2]Department of Biological Sciences, Bauru School of Dentistry, University of São Paulo, Bauru, SP, Brazil

[3]Department of Physiology, Development and Neuroscience, University of Cambridge, Cambridge, UK

Correspondence to: J. Michael Edwardson, Department of Pharmacology, University of Cambridge, Tennis Court Road, Cambridge CB2 1PD, UK; e-mail, jme1000@cam.ac.uk, or Marília Afonso Rabelo Buzalaf, Department of Biological Sciences, Bauru School of Dentistry, University of São Paulo, Alameda Octávio Pinheiro Brisolla, 9-75, Bauru-SP, Brazil 17012-901; e-mail: mbuzalaf@fob.usp.br

Abbreviations: AFM, atomic force microscopy; CFTR, cystic fibrosis transmembrane conductance regulator; ENaC, epithelial Na^+ channel; HEPES, 4-(2-hydroxyethyl)-1-piperazineethanesulfonic acid; IBMX, 3-isobutyl-1-methylxanthine; I_{sc}, short-circuit current; NKCC, Na-K-Cl co-transporter; R_t, transepithelial resistance; SEM, standard error of the mean.

ABSTRACT: Fluoride exposure is widespread, with drinking water commonly containing natural and artificially added sources of the ion. Ingested fluoride undergoes absorption across the gastric and intestinal epithelia. Previous studies have reported adverse gastrointestinal effects with high levels of fluoride exposure. Here, we examined the effects of fluoride on the transepithelial ion transport and resistance of three intestinal epithelia. We used the Caco-2 cell line as a model of human intestinal epithelium, and rat and mouse colonic epithelia for purposes of comparison. Fluoride caused a concentration-dependent decline in forskolin-induced Cl^- secretion and transepithelial resistance of Caco-2 cell monolayers, with an IC_{50} for fluoride of about 3 mM for both parameters. In the presence of 5 mM fluoride, transepithelial resistance fell exponentially with time, with a $t_{1/2}$ of about 7 h. Subsequent imaging by immunofluorescence and scanning electron microscopy showed structural abnormalities in Caco-2 cell monolayers exposed to fluoride. The Young's modulus of the epithelium was not affected by fluoride, although proteomic analysis revealed changes in expression of a number of proteins, particularly those involved in cell-cell adhesion. In line with its effects on Caco-2 cell monolayers, fluoride, at 5 mM, also had profound effects on Cl^- secretion and transepithelial resistance of both rat and mouse colonic epithelia. Our results show that treatment with fluoride has major effects on the structure, function, and proteome of intestinal epithelia, but only at concentrations considerably higher than those likely to be encountered *in vivo*, when much lower fluoride doses are normally ingested on a chronic basis.

Keywords: fluoride; epithelial ion transport; gastrointestinal epithelia; atomic force microscopy; cell stiffness; proteomics

INTRODUCTION

Fluoride exposure is common worldwide. The anion occurs naturally and is also commonly added to drinking water, with current World Health Organization guidelines (2006) recommending levels of 1.5 mg/L. Dental caries is a significant healthcare problem, occurring in 46% of 15 year-olds in the UK, for example (Murray et al., 2015), and fluoride is widely known for its beneficial effects in combating this condition (Parnell et al., 2009). Inadequate levels of exposure to fluoride (<0.5 mg/L in drinking water) can result in increased predisposition to caries, while excessive intake is associated with dental, and at higher levels, skeletal, fluorosis (McDonagh et al., 2000). Although, water is often the predominant source of intake, dental hygiene products, food and teas can also contribute to fluoride ingestion (Fawell et al., 2006). Importantly, levels of fluoride exposure are inconsistent worldwide, with many countries such as India and China reporting endemic fluorosis (Jolly et al., 1969; Lyth, 1946) as a result of naturally elevated levels in drinking water.

Ingested fluoride undergoes rapid gastric absorption in a pH-dependent manner, as a result of the high lipid solubility of hydrogen fluoride (Gutknecht and Walter, 1981), and increasing acidity increases the rate of uptake (Whitford and Pashley, 1984). Other factors, such as recent food consumption or dietary calcium consumption, can limit fluoride absorption (Whitford, 1994). The remaining fluoride is mostly absorbed in the small intestine (Nopakun et al., 1989), with a rate independent of pH (Buzalaf and Whitford, 2011). Gastrointestinal toxicity has been observed with fluoride, and gastrointestinal symptoms have been reported in cases of skeletal fluorosis (Dasarathy et al., 1996). Chronic ingestion of fluoride has also been correlated with histologically observable damage to the gastric epithelium (Das et al., 1994). These studies, although small-scale, indicate that further study of the potential adverse effects of fluoride on the gastrointestinal tract is warranted.

The intestinal epithelium is highly specialized, with distinct apical and basolateral transporters, and this functional polarization facilitates a broad range of absorptive and secretory functions (Cuthbert et al., 1999). Na^+ acts as the lead ion for absorption, with the Na^+/K^+-ATPase producing an inward electrochemical gradient for Na^+. This gradient enables diffusion of Na^+ into the cell through epithelial Na^+ channels, which is accompanied by Cl^- and water movement. The Na-K-Cl co-transporter (NKCC1) moves Cl^- ions into the cell via secondary active transport, coupled with Na^+ and K^+. K^+ then passes through basolateral K^+ channels, which hyperpolarizes the cell, thereby increasing the driving force for Cl^- exit. Cl^- secretion through apical Ca^{2+}-activated chloride channels and the cystic fibrosis transmembrane conductance regulator (CFTR) is accompanied by Na^+ and water (Barrett and Keely, 2000). Elevations of intracellular cAMP promote secretory mechanisms by actions on CFTR, NKCC1 and the basolateral KvLQT1 K^+ channel (Cuthbert et al., 1999).

Tight junctions between gastrointestinal epithelial cells form a continuous barrier between apical and basolateral cell surfaces, and control transport via the paracellular pathway (Balda et al., 1992). Tight junctions determine the integrity and core physiological properties of epithelia, such as the nature of molecules and ions that can diffuse across. Their regulation allows these epithelial properties to undergo dynamic changes (Matter and Balda, 2003). Tight junction complexes are composed of three key components: integral proteins, such as zona occludens-1 (ZO-1), that traverse the intercellular space, plaque proteins that join the integral proteins to the cytoskeleton, and a diverse range of multifunctional nuclear/cytosolic proteins (Schneeberger and Lynch, 2004). The ‘tightness’ or permeability of these junctions to ions is often measured via transepithelial resistance (R_t). As a result of the need for extensive absorption and secretion, the gastrointestinal tract has a relatively low R_t, with the exception of the terminal colonic regions (Anderson and Van Itallie, 2009).

The concentrations of fluoride required to produce toxic effects on the gastrointestinal tract, and importantly whether such concentrations are reached *in vivo*, are unclear. Here, we studied the effects of fluoride on the structure, function, and proteome of a model colonic epithelial cell line, the human Caco-2 cell line, and also on transepithelial ion transport in rat and mouse colonic epithelia. We observed profound structural and functional effects of fluoride; however, these effects were produced at fluoride concentrations that are unlikely to be encountered *in vivo*.

MATERIALS AND METHODS

Cell Culture

Caco-2 cells were cultured in Dulbecco's Modified Eagle's Medium (Life Technologies), containing 10% fetal bovine serum, 1% penicillin and 1% streptomycin at 37°C in an atmosphere of 5% CO_2/95% air. For polarized monolayer formation, cells were seeded into Snapwell™ inserts (Corning), which contained a 12-mm diameter polycarbonate membrane with 0.4-µm diameter pores. Inserts were placed in 6-well plates with 1.5 mL and 4 mL of medium on the apical and basolateral sides of the monolayers, respectively. Cells were cultured for 14-16 days to allow the formation of a tight, polarized epithelium. Note that although the Caco-2 cell line was originally derived from a human colon adenocarcinoma, the characteristics of the cells in culture depend heavily on culture conditions and are often more similar to those of small intestinal enterocytes (Sambuy et al., 2005). For this reason, we regard the Caco-2 cell monolayers as a model of a human intestinal epithelium in general, rather than of a colonic epithelium in particular.

Preparation of Rat and Mouse Colonic Epithelia

Wild type rats and mice of mixed weight, age and sex were used to provide sections of colonic tissue. Following cervical dislocation, the peritoneum was dissected away; the colon

was removed and the tissue was maintained in aerated (5% CO_2/95% O_2) Krebs-Henseleit solution (117 mM NaCl, 4.7 mM KCl, 2.5 mM $CaCl_2$, 1.2 mM $MgSO_4$, 1.2 mM KH_2PO_4, 24.8 mM $NaHCO_3$, 11.1 mM glucose, pH 7.4). The section of colon below the caecum was divided into three or four 1.5-cm segments, which were incised along the mesenteric line. The serosa and muscularis mucosae were then removed using watchmaker's forceps.

Measurement of Transepithelial Ion Transport and Resistance

Voltage clamps (DVC-1000 Epithelial Voltage/Current Clamp, World Precision Instruments) were calibrated before each experiment (Input/Offset and Fluid RES compensation set to 0.0). Snapwell™ inserts with confluent Caco-2 cell monolayers were transferred to Ussing chambers (Ussing and Zerahn, 1951) with a 1.13 cm^2 aperture (World Precision Instruments). For colonic epithelia, the aperture was 0.2 cm^2. The monolayers or epithelia were bathed on both apical and basolateral sides with 20 mL of Krebs-Henseleit solution at 37°C, and continuously aerated with 5% CO_2/95% O_2. Chambers were left for 10-30 min to equilibrate once voltage clamping had begun. PowerLab 2/25 software (ADInstruments) was used to record the short-circuit current (I_{sc}) across the epithelium, with one data point per second plotted on continuous axes of I_{sc} versus time. All traces were recorded using PowerLab hardware with LabChart software, and data were analysed using Microsoft Excel software. Transepithelial resistance (R_t) was measured via changes in I_{sc} during 5-s pulses to a 2-mV transepithelial voltage every 30 s, according to Ohm's law, ($R_t=V/I$). 3-isobutyl-1-methylxanthine (IBMX; Sigma), amiloride (Sigma) and furosemide (Sigma) were dissolved in water, while forskolin (Calbiochem) was dissolved in 95% ethanol. Drugs were diluted to appropriate final concentrations in Krebs-Henseleit solution.

Data Analysis

All traces were viewed on a LabChart Reader, and data were recorded in a Microsoft Excel 2013 spreadsheet for further analysis. For all data, mean and standard error of the mean (SEM) were calculated.

Concentration-response curves for the effects of fluoride or forskolin on ΔI_{sc} and for the effect of fluoride on R_t were plotted in Excel 2013. Data were fitted to the following 4-parameter logistic equation using the maximum likelihood approach:

$$E = \frac{Min - Max}{\left(1 + \left(\frac{[A]}{10^{-pIC_{50}}}\right)^{n_H}\right)} + Max$$

where E is the response (ΔI_{sc} or R_t), [A] is [NaF] or [forskolin], Min is the response when [A]=0, Max is the response when [A]=∞, pIC_{50}=$-log(IC_{50})$,and n_H is the Hill Coefficient.

For these data an additional model was used for the residual error variance (RUV):

$$RUV_i = \alpha^2 \hat{y}_i^{\gamma}$$

where RUV_i is the residual unexplained variance for data point I, α^2 is a variance parameter, and $\hat{y}_i$ is the modeled response for data point i. γ defines the relationship between residual error and response; e.g. when $\gamma = 0$, residual error is constant (i.e. homoscedastic) and when $\gamma = 2$, the standard deviation of the residual error is directly proportional to the response (i.e. the coefficient of variation is a constant).

The Excel Solver function was used to minimize the value of extended least squares to fit the curves, integrating both of the above models. GraphPad Prism 6 or 7 was used to plot exponential decline curves of R_t and ΔI_{sc} in time-course experiments, to carry out linear regression and to compare data sets with unpaired t-tests. Two-way ANOVA tests with Bonferroni's post-hoc tests were used to compare the difference in means between control and fluoride exposure data for experiments on colonic epithelia. One-way ANOVA tests with

Tukey's post-hoc tests were used to determine how means changed during each protocol. Significance was taken at $P<0.05$.

Scanning Electron Microscopy

Cell monolayers on polycarbonate membranes (excised from Snapwell™ inserts) and supported on coverslips were quench-frozen by plunging, cell face first, into melting propane cooled in liquid nitrogen. Monolayers were freeze-dried in a modified Edwards 306 Auto 306 carbon coating unit (Warley and Skepper, 2000). After drying, the cells were coated with carbon and attached to scanning electron microscopy stubs with colloidal silver. The cells were coated with 10 nm of gold in a Quorum/Emitech K575X sputter coater and viewed in an FEL-Philips XL30 FEGSEM at 5 kV.

Immunofluorescence

Cell monolayers were fixed in 4% paraformaldehyde in phosphate-buffered saline, and permeabilized by treatment with 0.05% saponin in the same buffer containing 0.2% gelatin. Monolayers were incubated in permeabilization buffer containing rat monoclonal anti-zona occludens-1 (ZO-1) monoclonal antibody (eBioscience), followed by fluorescein isothiocyanate-conjugated rabbit anti-rat secondary antibody (Sigma). The cells were then subjected to fluorescence microscopy.

Measurement of Young's Modulus

The stiffness of living Caco-2 epithelial cell monolayers, as represented by their Young's modulus, was determined using an atomic force microscopy (AFM) nano-indentation technique (Heinz and Hoh, 1999; Kasas and Dietler, 2008). The Young's modulus was calculated via the force that had to be exerted to indent the cell membrane by a fixed distance. Measurements were conducted at room temperature using a scanning probe microscope (BioScope® I SPM, Bruker) integrated into an inverted microscope (Axiovert 135, Zeiss).

Cell monolayers growing in 6-well culture plates were washed with 4-(2-hydroxyethyl)-1-piperazineethanesulfonic acid- (HEPES)-buffered saline solution (135 mM NaCl, 5 mM KCl, 1 mM $MgCl_2$, 1 mM $CaCl_2$, 10 mM HEPES, pH 7.4) and bathed in the same solution during experiments. Measurements were performed using soft cantilevers (spring constant, <20 pN/nm; Novascan) with a polystyrene sphere (diameter, 10 μm) as the tip. A maximal loading force of 10 nN was applied. For each monolayer, 9 cell areas were chosen and 25 force-distance curves were collected for each area. AFM data were collected with NanoScope software 5.31 (Bruker). Young's modulus values were calculated from force-distance curves using AtomicJ Software (Hermanowicz *et al.*, 2014). Average Young's modulus values were calculated for each cell area, and these values were in turn averaged to produce a single value for each monolayer. Four monolayers were analysed for each condition (i.e. with or without fluoride treatment).

Proteomic Analysis of Caco-2 Cells

Caco-2 cell monolayers were either untreated (control) or exposed to 5 mM fluoride (as NaF) for 24 h. Experiments were conducted in quintuplicate. Membrane proteins were extracted using a Mem-PER™ eukaryotic membrane protein extraction kit (Thermo Scientific). The fraction containing hydrophobic proteins was collected and the proteins were purified using detergent removal spin columns (Thermo Scientific). Proteins were extracted, reduced, alkylated and digested as previously described (Antonio et al., 2017), and then analyzed using a nanoAcquity UPLC-XEVO QToF mass spectrometry system (Lima Leite et al., 2014). Differences in expression between the groups were assessed using PLGS software and expressed as $P<0.05$ for down-regulated and $(1-P)>0.05$ for up-regulated proteins. Functional enrichment was analysed using ClueGo, a Cytoscape plugin. For each comparison, bioinformatics analysis was performed, as described previously (Orchard, 2012; Bauer-Mehren, 2013; Millan, 2013; Lima Leite et al., 2014).

RESULTS

Effect of Fluoride on Caco-2 Cell Monolayers

Caco-2 cells were cultured for 14-16 days on polycarbonate membranes to produce polarized monolayers, and transepithelial ion transport was measured using short circuit current (I_{sc}) recordings in Ussing chambers. Addition of forskolin (10^{-5} M) to both sides of the monolayer, in the presence of the phosphodiesterase inhibitor IBMX (10^{-4} M), was used to elevate intracellular cAMP concentration. Forskolin treatment caused a transient rise in I_{sc} (asterisk), through a cAMP-dependent stimulation of Cl^- transport via CFTR [Fig. 1(A)]. The transient nature of the effect of forskolin on Caco-2 monolayers has been observed previously (Zhu et al., 2005; Jantarajit et al., 2017) and may be a result of a lack of hyperpolarising K^+ channels in the basolateral membrane, which sustain prolonged secretory responses in other epithelia (see below). The forskolin-stimulated I_{sc} in untreated monolayers (transporting area 1.13 cm^2) was typically about 2 $\mu A/cm^2$, and the transepithelial resistance was about 350 Ω cm^2. Preincubation of the monolayers in medium containing various concentrations of fluoride for 48 h resulted in a concentration-dependent reduction in forskolin-stimulated I_{sc} [Fig. 1(B)], with an IC_{50} for fluoride of 3.1 mM (95% confidence interval, 2.9-3.3 mM). Transepithelial resistance (R_t) was also reduced in a concentration-dependent manner by fluoride treatment over a 48-h period [Fig. 1(C)], with an identical IC_{50} of 3.1 mM (95% confidence interval, 2.6-3.7 mM). The time-course of the effect of fluoride (5 mM) on R_t was exponential, with a $t_{1/2}$ of 7.08±2.98 h [Fig. 1(D)].

To probe the effect of fluoride on the fine structure of the Caco-2 cell monolayer, we used scanning electron microscopy. Confluent monolayers were either untreated or treated for 48 h with 5 mM fluoride, conditions that reduced transepithelial resistance to zero (see above). Typical scanning electron micrographs are shown in Fig. 2. As can be seen, the apical

surface of the control monolayer was almost flat, although individual cells could just be discerned [Fig. 2(A)]. In contrast, the surface of the fluoride-treated monolayer was highly disrupted, with apparent gaps in the monolayer and the presence of rounded cells [Fig. 2(B)]. This observation suggested that the tight junctions between the cells might have been disrupted by fluoride treatment. To test this possibility, we examined the distribution of the tight junction protein ZO-1 by immunofluorescence [Fig. 3]. We found that the control monolayer had a regular pavement-like appearance, with polygonal staining for ZO-1 [Fig. 3(A)]. In contrast, the fluoride-treated monolayer showed a more irregular ZO-1 staining pattern [Fig. 3(B)]. Further, the polygons bounded by ZO-1 were larger than in the control monolayer and often enclosed more than one cell, as indicated by the nuclei that were visible in the image (arrows). Fluoride, therefore, disrupted the tight junction arrangement in Caco-2 cell monolayers.

We also examined the effect of fluoride on the Young's modulus of Caco-2 epithelia by nanoindentation using AFM. Cell monolayers growing in plastic culture dishes were either incubated with 5 mM fluoride for 48 h or left untreated. At the end of the incubation period, the mechanical properties of cells within the monolayers were measured using AFM probes with spherical tips as mechanosensors. The AFM probe was lowered onto the cell monolayer until it made contact with the apical membrane. It was then allowed to indent the cells for ~300 nm, which resulted in bending of the cantilever upon which the tip is mounted. This bending was amplified by a laser beam projected onto the back of the cantilever, and the reflected beam was monitored by a split photodiode. The tip was retracted from the cell, and multiple cycles of indentation and retraction were carried out. A force-distance curve was plotted for each cycle, relating the bending of the cantilever (or the applied force) to the position of the sample. The Young's modulus of each cell was then calculated from the slope of this curve. The values of Young's modulus for control and fluoride-treated cells were

12.9±3.3 (n=4) and 21.0±3.1; (n=4) kPa, respectively (P=0.12). Hence, fluoride treatment did not significantly affect the Young's modulus of the cells, as we reported recently for M-1 mouse kidney cortical collecting duct epithelia (Antonio et al., 2017). It is noteworthy that the Young's modulus of the Caco-2 cell monolayer is substantially greater than the 1 kPa obtained for M-1 cell monolayers, although it is similar to the value of about 25 kPa reported for MDCK cell monolayers (Schulze et al., 2017).

Effect of Fluoride on Rat Colonic Epithelia

As mentioned above, Caco-2 cell monolayers are not an ideal model of a colonic epithelium. Hence, we sought to determine the effect of fluoride on *ex vivo* colonic epithelia. Representative cumulative concentration-response results for forskolin acting on a rat colonic epithelium are shown in Figure 4(A). Initially, amiloride (10^{-5} M) was added to the apical side of the epithelium to inhibit Na^+ entry through epithelial Na^+ channels (ENaCs). In fact, amiloride did not evoke a response (arrowhead), indicating that electrogenic Na^+ transport does not contribute to the I_{sc} in this epithelium. Addition of forskolin (10^{-5} M) to both sides of the epithelium (asterisks) caused a long-lasting increase in I_{sc}, in contrast to the transient response seen in Caco-2 cell monolayers (above). This is likely because basolateral K^+ channels in the native colonic epithelial cells have a greater ability to maintain a hyperpolarised state, and thus to maintain Cl^- secretion, compared with Caco-2 monolayers (Cuthbert et al., 1999). Forskolin caused a concentration-dependent increase in I_{sc}, peaking at about 125 $\mu A/cm^2$ [Fig. 4(A)], far greater than the 2 $\mu A/cm^2$ seen in Caco-2 cell monolayers (above). Addition of furosemide (10^{-4} M) to the basolateral side of the epithelium at the end of the experiment almost abolished the forskolin-induced increase in I_{sc} (circle), consistent with its action as a blocker of NKCC1. Pre-treatment of the epithelia for 30 min with 5 mM fluoride almost completely abolished the I_{sc} response to forskolin [Fig. 4(B)]. In addition, the I_{sc} responses to the voltage pulses grew progressively during the course of the experiment (~1

h), indicating that R_t was falling, likely because of a continuing effect of fluoride. Combined data for forskolin acting on control and fluoride-treated rat colonic epithelia are shown in Figure 4(C). The parameters of the curve for the control epithelia were EC_{50}=3.33 x 10^{-7} M, Min=-2.87 μA, Max=26.93 μA, Hill coefficient 0.95. The effect of fluoride on forskolin-stimulated I_{sc} was highly significant (two-way ANOVA; P<0.0001). In fact, for the fluoride-treated tissues, forskolin did not cause a positive change in I_{sc}. The resistance of control rat colonic epithelia was about 35 Ω cm^2, far lower than the value for Caco-2 cell monolayers, and remained constant for up to 3.5 h [Fig. 4(D)]. Consistent with its effect on forskolin-stimulated I_{sc}, fluoride caused a dramatic reduction in R_t over a 30-min incubation period, and there was no significant further decrease over a subsequent 3-h incubation (one-way ANOVA with Tukey's post-hoc test; $P \geq 0.05$). R_t for fluoride-treated epithelia was significantly lower at all time points than R_t for control epithelia ($P<0.0001$).

Effect of Fluoride on Mouse Colonic Epithelia

As in the rat colonic epithelia, forskolin caused a concentration-dependent increase in I_{sc} in mouse colonic epithelia, rising to about 80 μA/cm^2 at 10^{-5} M forskolin [Fig. 5(A)]. Again, pre-treatment of the epithelia for 30 min with 5 mM fluoride almost completely abolished the I_{sc} response to forskolin. The parameters of the curve for the control epithelia were EC_{50}=2.71 x 10^{-7} M, Hill coefficient=2.21, and for fluoride-treated epithelia the parameters were EC_{50}=2.93 x 10^{-7} M, Hill coefficient=12.08. After fluoride treatment, the maximum response to forskolin was reduced by 78% from 77 μA/cm^2 to 17 μA/cm^2. As with rat epithelia, the effect of fluoride on forskolin-stimulated I_{sc} was highly significant (two-way ANOVA; P<0.0001). The resistance of control mouse colonic epithelia was about 50 Ω cm^2 (i.e. higher than that in the rat colonic epithelia), and again remained constant for up to 3.5 h [Fig. 5(B)]. Fluoride reduced R_t during a 30-min incubation period, and again there was no significant further decrease over the subsequent 3 h (one-way ANOVA with Tukey's post-

hoc test; $P \geq 0.05$). In mouse epithelia treated with fluoride (n= 5), transepithelial resistance was lower than in control epithelia (n=2). R_t for fluoride-treated epithelia was significantly lower at all time points than R_t for control epithelia ($P<0.0001$).

Proteomic Analysis

Caco-2 cell monolayers were either untreated (control) or exposed to 5 mM fluoride for 24 h. Comparative analysis showed 5 and 103 proteins up- and down-regulated, respectively, in the fluoride-treated group compared with control [Table SI]. The numbers of proteins exclusively expressed in the control and fluoride-treated groups were 229 [Table SII] and 113 [Table SIII], respectively. GO analysis showed that proteins with altered expression were most commonly related to the "homophilic cell adhesion via plasma membrane adhesion molecules" term, with a 14% frequency. In addition, 8% of the proteins were related to "response to unfolded protein", while 7% were related to "pyridine-containing compound metabolic process". Exposure to fluoride changed the expression of various proteins related to cell motility and adhesion. The expression of proteins related to actin binding, such as various isoforms of alpha-actinin was increased, while the expression of various isoforms of tubulin and actin was decreased. In addition, some proteins related to cell-matrix and cell-cell adhesion were uniquely identified in the group exposed to fluoride, such as integrin beta-4 fragment (J3KSH9), while others were uniquely identified in the control group, such as vinculin (P18206) and multiple isoforms of protocadherin. Furthermore, exposure to fluoride reduced the expression of various proteins related to different steps of protein synthesis and folding, as depicted in the sub-network shown in Figure 6, where many proteins with altered expression interacted with SNW domain-containing protein 1 (Q13573), which is involved in transcriptional regulation. Among the interacting proteins are 78 kDa glucose-regulated protein (GRP78; P11021) and elongation factor 1-alpha 1 (P68104), which were down-regulated by fluoride, and 116 kDa U5 small nuclear ribonucleoprotein component (Q15029)

and nuclear receptor corepressor 2 (Q9Y618), which were absent after exposure to fluoride. Other proteins related to folding that were also reduced in sub-network are endoplasmin (P14625), down-regulated by fluoride and T-complex protein 1 subunit beta (P78371) absent upon exposure to fluoride.

DISCUSSION

We have investigated the effects of fluoride on three types of intestinal epithelium: Caco-2 cell monolayers, and rat and mouse colonic epithelia. We found that fluoride reduced forskolin-stimulated I_{sc} and R_t in all three epithelia. In Caco-2 cell monolayers, these functional effects of fluoride were accompanied by perturbations of the morphology of tight junctions between the cells, as revealed by both scanning electron microscopy and anti-ZO-1 immunofluorescence. In this context, our finding that the expression of alpha-actinin-4 (P O43707) was increased upon exposure to fluoride is interesting. This protein is involved in tight junction assembly in epithelial cells probably through interaction with MICALL2; specifically, it links MICALL2 to the actin cytoskeleton and recruits it to tight junctions (UNIPROT).

The Caco-2 adenocarcinoma cell line forms monolayers that are of similar morphology to native enterocytes (Hidalgo et al., 1989), and polymerase chain reaction analysis has shown that transporter expression is similar to that in the small intestine (Maubon et al., 2007). In our experiments, fluoride reduced forskolin-stimulated I_{sc} and R_t over identical concentration ranges (IC_{50}, 3.1 mM). Hence, the Caco-2 cell monolayers are considerably less sensitive to fluoride than M-1 mouse kidney cortical collecting duct epithelia, in which both I_{sc} and R_t are reduced to zero at 1 mM fluoride (IC_{50}, 300 μM; Antonio et al., 2017). Although its molecular basis is unclear and the first insights into this aspect have only been

recently reported (Melo et al., 2017), this difference might reflect the fact that the intestinal epithelium is the first barrier encountered by ingested fluoride.

Interestingly, while we found that both I_{sc} and R_t in Caco-2 cell monolayers were reduced to zero at 5 mM fluoride, others have shown that cell viability is unaffected by fluoride at concentrations up to 5.2 mM (Rocha et al., 2013). This discrepancy suggests that changes in transepithelial ion transport and resistance are particularly sensitive cytotoxic effects that are manifest before cell viability is compromised (Narai et al., 1997). In support of this suggestion, Wang et al. (2001) found a diminished R_t in endothelial cells exposed to 20 mM NaF after 10 min, despite cell viability assays indicating no cytotoxicity at 2 h. The fact that forskolin-stimulated I_{sc} and R_t were equally sensitive to fluoride suggest that the two effects have a common cause. The observed effects on tight junction morphology could account for the reduced R_t, which in turn would reduce the electrogenic ion transport across the epithelium, thereby explaining the reduction in I_{sc}.

Various intracellular targets of fluoride have been identified in previous studies. There have been several reports of effects on the cytoskeleton; for example, endothelial cells exposed to fluoride undergo contraction and increased intercellular separation (similar to the effect observed in the present study), which coincides with increased myosin light chain phosphorylation (Wang et al., 2001). However, the fact that fluoride did not affect cell stiffness in our experiments would appear to rule out a significant effect on the cytoskeleton of Caco-2 cells. A 24-h exposure to fluoride (2.1-8.4 mM) induced DNA damage and cytotoxicity in human embryo hepatocytes (Wang et al., 2004). Further, in human oral mucosal fibroblasts, fluoride caused ATP depletion, disturbed protein synthesis and diminished mitochondrial function in a concentration-dependent manner above 4 mM (Jeng et al., 1998). The observed reduction in the number or amount of proteins identified upon treatment with fluoride suggests that protein synthesis and folding had been adversely

affected [Tables SI-SIII, Fig. 6]. Fluoride may also directly inhibit ion transport through effects on the Na^+/K^+-ATPase (Murphy and Hoover, 1992), or a reduction in intracellular ATP levels, as seen in macrophages at physiologically relevant plasma fluoride concentrations (Gutowska et al., 2010). In the present study, expression of two isoforms of ATP synthase was reduced upon exposure to fluoride [Table SI]. Numerous intestinal epithelial transporters can be modulated via phosphorylation (Barrett and Keely, 2000); hence, the known actions of fluoride on cellular phosphatases and kinases, either direct or via intracellular pathways, could result in altered ionic transport. It has been reported, for instance, that fluoride can inhibit renal phosphatases at micromolar levels (Partanen, 2002), and exert effects on G-protein signaling, protein kinases A and C, and tyrosine kinase in human lung epithelial cells (Refsnes et al., 2003).

Current World Health Organization guidelines (2006) recommend water fluoride levels of 1.5 mg/L (~80 μM), which is significantly lower than the concentrations producing effects in our experiments. The highest groundwater fluoride level observed in India, 48 mg/L (2.5 mM; Fawell et al., 2006), approaches our IC_{50} in Caco-2 cell monolayers, but any meaningful comparison would have to be based on the assumption that the epithelium would be directly exposed to the imbibed fluid. The fact that 5 mM fluoride had similar effects on rat and mouse colonic epithelia to those on Caco-2 cell monolayers suggests that the results obtained with the intestinal cell line are relevant to the behavior of intestinal epithelia *in vivo*. On the other hand, we need to recognize that our experiments involved only exposure to fluoride for a maximum of 72 h, raising the possibility that our results may not be directly applicable to the situation where people are exposed chronically to low-levels of fluoride in drinking water.

In conclusion, our results show that fluoride exposure induces changes in the structure, function and proteome of intestinal epithelia, but only at concentrations higher than those likely to be encountered under normal circumstances.

Acknowledgements: We are grateful to Dr. Jeremy Skepper of the Cambridge Advanced Imaging Centre for his expert assistance with the scanning electron microscopy. This work was supported by a grant from the CAPES Science Without Borders Programme (Brazil). P.J. and J.M.E. were supported by Kidney Research UK.

REFERENCES

Anderson JM, Van Itallie CM. 2009. Physiology and function of the tight junction. Cold Spring Harb Perspect Biol 1:a002584.

Antonio LS, Jeggle P, MacVinish LJ, Bartram JC, Miller H, Jarvis GE, Levy FM, Santesso MR, Leite AL, Oliveira RC, Buzalaf MAR, Edwardson JM (2017) The effect of fluoride on the structure, function and proteome of a renal epithelial cell monolayer. Env Toxicol 32:1455-1467.

Balda MS, Fallon MB, Van Itallie CM, Anderson JM. 1992. Structure, regulation, and pathophysiology of tight junctions in the gastrointestinal tract. Yale J Biol Med 65:725-735.

Barrett KE, Keely SJ. 2000. Chloride secretion by the intestinal epithelium: molecular basis and regulatory aspects. Annu Rev Physiol 62:535-572.

Bauer-Mehren A (2013) Integration of genomic information with biological networks using Cytoscape. Meth Mol Biol 1021:7-61.

Buzalaf MAR, Whitford GM. 2011. Fluoride metabolism. In: Buzalaf MAR (ed.) Fluoride and the Oral Environment. Monogr Oral Sci 22:20-36. Basel: Karger.

Cuthbert AW, Hickman ME, MacVinish LJ. 1999. Formal analysis of electrogenic sodium, potassium, chloride and bicarbonate transport in mouse colon epithelium. Br J Pharmacol 126:358-364.

Das TK, Susheela AK, Gupta IP, Dasarathy S, Tandon RK. 1994. Toxic effects of chronic fluoride ingestion on the upper gastrointestinal tract. J Clin Gastroenterol 18:194-199.

Dasarathy S, Das TK, Gupta IP, Susheela AK, Tandon RK. 1996. Gastroduodenal manifestations in patients with skeletal fluorosis. J Gastroenterol 31:333-337.

Fawell J, Bailey K, Chilton J, Dahi E, Fewtrell L, Magaia Y. 2006. Fluoride in drinking-water, IWA Publishing, London.

Gutknecht J, Walter A. 1981. Hydrofluoric acid and nitric-acid transport through lipid bilayer-membranes. Biochim Biophys Acta 644:153-156.

Gutowska I, Baranowska-Bosiacka I, Baśkiewicz M, Milo B, Siennicka A, Marchlewicz M, Wiszniewska B, Machaliński B, Stachowska E. 2010. Fluoride as a pro-inflammatory factor and inhibitor of ATP bioavailability in differentiated human THP1 monocytic cells. Toxicol Lett 196:74-79.

Heinz WF, Hoh JH. 1999. Spatially resolved force spectroscopy of biological surfaces using the atomic force microscope. Trends Biotechnol 17:143-150.

Hermanowicz P, Sarna M, Burda K, Gabrys H. 2014. AtomicJ: An open source software for analysis of force curves. Rev Sci Instrum 85:063703.

Hidalgo IL, Raub TJ, Borchardt RT. 1989. Characterization of the human colon carcinoma cell line (Caco-2) as a model system for intestinal epithelial permeability. Gastroenterology 96:736-749.

Jantarajit W, Lertsuwan K, Teerapornpuntakit J, Krishnamra N, Charoenphandhu N. 2017. CFTR-mediated anion secretion across intestinal epithelium-like Caco-2 monolayer under PTH stimulation is dependent on intermediate conductance K^+ channels. Am J Physiol Cell Physiol 313:C118-C129.

Jeng JH, Hsieh CC, Lan WH, Chang MC, Lin SK, Hahn LJ, Kuo MY. 1998. Cytotoxicity of sodium fluoride on human oral mucosal fibroblasts and its mechanisms. Cell Biol Toxicol 14:383-389.

Jolly SS, Singh BM, Mathur OC. 1969. Endemic fluorosis in Punjab (India). Am J Med 47:553-563.

Kasas S, Dietler G. 2008. Probing nanomechanical properties from biomolecules to living cells. Pflügers Arch 456:13-27.

Lima Leite A, Gualiume Vaz Madureira Lobo J, Barbosa da Silva Pereira HA, Silva Fernandes M, Martini T, Zucki F, et al. (2014) Proteomic analysis of gastrocnemius muscle in rats with streptozotocin-induced diabetes and chronically exposed to fluoride. PLoS One 9:e106646.

Lyth, O. 1946. Endemic fluorosis in Kweichow, China. Lancet 1:233-235.

McDonagh MS, Whiting PF, Wilson PM, Sutton AJ, Chestnutt I, Cooper J, Misso K, Bradley M, Treasure E, Kleijnen J. 2000. Systematic review of water fluoridation. Brit Med J 321, 855-859.

Matter K, Balda MS. 2003. Functional analysis of tight junctions. Methods 30:228-234.

Maubon N, Le Vée M, Fossati L, Audry M, Le Ferrec E, Bolze S, Fardel O. 2007. Analysis of drug transporter expression in human intestinal Caco-2 cells by real-time PCR. Fundam Clin Pharmacol 21:659-663.

Melo CGS, Perles JVCM, Zanoni JN, Souza SRG, Santos EX, Leite AL, Heubel AD, E Souza CO, Souza JG, Buzalaf MAR. 2017. Enteric innervation combined with proteomics for the eveluation of the effects of chronic fluoride exposure on the duodenum of rats. Sci Rep 7:1070.

Millan PP (2013) Visualization and analysis of biological networks. Meth Mol Biol 1021:63-88.

Murphy AJ, Hoover JC. 1992. Inhibition of the Na,K-ATPase by fluoride. Parallels with its inhibition of the sarcoplasmic reticulum CaATPase. J Biol Chem 267:16995-16700.

Murray JJ, Vernazza CR, Holmes RD. 2015. Forty years of national surveys: An overview of children's dental health from 1973-2013. Brit Dent J 219:281-285.

Narai A, Arai S, Shimizu M. 1997. Rapid decrease in transepithelial electrical resistance of human intestinal Caco-2 cell monolayers by cytotoxic membrane perturbents. Toxicol In Vitro 11:347-354.

Nopakun J, Messer HH, Voller V. 1989. Fluoride absorption from the gastrointestinal tract of rats. J Nutr 119:1411-1417.

Orchard S. 2012. Molecular interaction databases. Proteomics 12:1656-1662.

Parnell C, Whelton H, O'Mullane D, 2009. Water fluoridation. Eur Arch Paediatr Dent Off J Eur Acad Paediatr Dent 10:141-148.

Partanen S. 2002. Inhibition of human renal acid phosphatases by nephrotoxic micromolar concentrations of fluoride. Exp Toxicol Pathol 54:231-237.

Refsnes M, Schwarze PE, Holme JA, Låg M. 2003. Fluoride-induced apoptosis in human epithelial lung cells (A549 cells): role of different G protein-linked signal systems. Hum Exp Toxicol 22:111-123.

Rocha RA, Devesa V, Vélez D. 2013. In vitro study of intestinal transport of fluoride using the Caco-2 cell line. Food Chem Toxicol 55:156-163.

Sambuy Y, De Angelis I, Ranaldi G, Scarino ML, Stammati A, Zucco F. 2005. The Caco-2 cell line as a model of the intestinal barrier: influence of cell and culture-related factors on Caco-2 cell functional characteristics. Cell Biol Toxicol 21:1-26.

Schneeberger EE, Lynch RD. 2004. The tight junction: a multifunctional complex. Am J Physiol Cell Physiol 286:C1213-1228.

Schulze KD, Zehnder SM, Urueña JM, Bhattacharjee T, Sawyer WG, Angelini TE. 2017. Elastic modulus and hydraulic permeability of MDCK monolayers. J Biomech 53:210-213.

Ussing HH, Zerahn K. 1951. Active transport of sodium as the source of electric current in the short-circuited isolated frog skin. Acta Physiol Scand 23:110-127.

Wang AG, Xia T, Chu QL, Zhang M, Liu F, Chen XM, Yang KD. 2004. Effects of fluoride on lipid peroxidation, DNA damage and apoptosis in human embryo hepatocytes. Biomed Environ Sci 17:217-222.

Wang P, Verin AD, Birukova A, Gilbert-McClain LI, Jacobs K, Garcia JG. 2001. Mechanisms of sodium fluoride-induced endothelial cell barrier dysfunction: role of MLC phosphorylation. Am J Physiol Lung Cell Mol Physiol 281:L1472-L1483.

Warley A, Skepper JN. 2000. Long freeze-drying times are not necessary during the preparation of thin sections for X-ray microanalysis. J Microsc 198:116-123.

Whitford GM. 1994. Effects of plasma fluoride and dietary calcium concentrations on GI absorption and secretion of fluoride in the rat. Calcif Tissue Int 54:421-425.

Whitford GM, Pashley DH. 1984. Fluoride absorption: the influence of gastric acidity. Calcif Tissue Int 36:302-307.

World Health Organisation. 2006. Guidelines for drinking-water quality. First addendum to third edition, Volume 1, Recommendations, Geneva, World Health Organization.

Zhu JX, Zhang GH, Yang Y, Rowlands DK, Wong HYC, Tsang LL, Chung YW, Chan HC. 2005. Activation of apical CFTR and basolateral Ca^{2+}-activated K^{+} channels by tetramethylpyrazine in Caco-2 cell line. Eur J Pharmacol 510:187-195.

Fig. 1. Effect of fluoride on the function of Caco-2 cell monolayers. (A) Representative response to forskolin, added at the asterisk. Transepithelial resistance (R_t) was measured via changes in I_{sc} during 5-s pulses to a 2-mV transepithelial voltage every 30 s. (B) Relationship between forskolin-stimulated I_{sc} and fluoride concentration. Bars show SEM (n=4-14). The dashed line shows the IC_{50} value. (C) Relationship between R_t and fluoride concentration. Bars show SEM (n=4-14). The dashed line shows the IC_{50} value. (D) Time-course of the effect of fluoride on R_t. Bars show SEM (n=3-15).

Fig. 2. Effect of fluoride treatment on epithelial structure. Representative scanning electron micrographs of the apical surface of a control epithelium (A) and an epithelium treated for 48 h with 5 mM fluoride (B). Scale bars, 5 μm.

Fig. 3. Effect of fluoride on tight junction integrity. Immunofluorescence images showing the distribution of ZO-1 in a control epithelium (A) and in an epithelium treated for 48 h with 5 mM fluoride (B). Arrows indicate areas enclosed by ZO-1 that contain more than one nucleus. Scale bar, 50 μm.

Fig. 4. Effect of fluoride on the function of rat colonic epithelia. (A) Representative cumulative concentration-response data for forskolin acting on a control rat colonic epithelium. Amiloride (10^{-5} M) was added at the arrowhead to block ENaC. Increasing concentrations of forskolin (10^{-7} M, 3 x 10^{-7} M, 10^{-6} M, 3 x 10^{-6} M and 10^{-5} M) were then added at the asterisks. Finally, furosemide (10^{-4} M) was added at the circle to block NKCC1. Transepithelial resistance (R_t) was measured via changes in I_{sc} during 5-s pulses to a 2-mV transepithelial voltage every 30 s. Time scale bar, 10 min. (B) Representative cumulative concentration-response data for forskolin acting on a rat colonic epithelium that had been pre-

treated with fluoride for 30 min. Drugs were added as in (A). Time scale bar, 10 min. (C) Relationship between I_{sc} and the concentration of forskolin in control (circles; n=11) and fluoride-treated (5 mM; squares; n=12) epithelia. Bars show SEM. Data were fitted to a 4-parameter logistic equation. Asterisks indicate a significant difference between control and fluoride (two-way ANOVA with Bonferroni's post-hoc test: ***, P<0.001; ****, P<0.0001). (D) Time-course of the effect of fluoride on R_t. Data are shown for control (circles; n=2) and fluoride-treated (5 mM; squares; n=6) epithelia. Bars show SEM. Asterisks indicate a significant difference between control and fluoride (two-way ANOVA with Bonferroni's post-hoc test: **, P<0.01; ****, P<0.0001).

Fig. 5. Effect of fluoride on the function of mouse colonic epithelia. (A) Relationship between I_{sc} and forskolin concentration in control (circles; n=31) and fluoride-treated (5 mM; squares; n=12) epithelia. Bars show SEM. Data were fitted to a 4-parameter logistic equation. Asterisks indicate a significant difference between control and fluoride (two-way ANOVA with Bonferroni's post-hoc test, ***P < 0.001, ****P < 0.0001). (B) Time-course of the effect of fluoride on R_t. Data are shown for control (diamonds; n=2) and fluoride-treated (5 mM; squares; n=5) epithelia. Bars show SEM. Asterisks indicate a significant difference between control and fluoride (two-way ANOVA with Bonferroni's post-hoc test: **, P<0.01; ****, P<0.0001).

Fig. 6. Subnetwork created by ClusterMark® to establish the interaction between proteins in Caco-2 cells identified as having differential expression in the fluoride-treated group compared with control. The color of the nodes indicates the differential expression of each protein, with its access code. The dark red nodes indicate proteins unique to the control. The nodes in gray indicate the interacting proteins predicted by CYTOSCAPE®, which were not

identified in the present study. The light red nodes indicate proteins downregulated in the fluoride-treated group. According to the UNIPROT data base, the proteins illustrated are: P78371: T-complex protein 1 subunit beta; Q5VW00: DDB1- and CUL4-associated factor 12-like protein 2; Q9Y618: Nuclear receptor corepressor 2; Q15029: 116 kDa U5 small nuclear ribonucleoprotein component; P06733: Alpha-enolase; P11021: 78 kDa glucose-regulated protein; P14625: Endoplasmin; P07437: Tubulin beta chain; P68104: Elongation factor 1-alpha 1; P68133: Actin, alpha skeletal muscle; O43823: A-kinase anchor protein 8; O15379: Histone deacetylase 3; O95503: Chromobox protein homolog 6; O94905: Erlin-2; Q13573: SNW domain-containing protein 1; Q96D17: tRNA pseudouridine(38/39) synthase; Q01534: Testis-specific Y-encoded protein 1; P17020: Zinc finger protein 16.

Figure 1

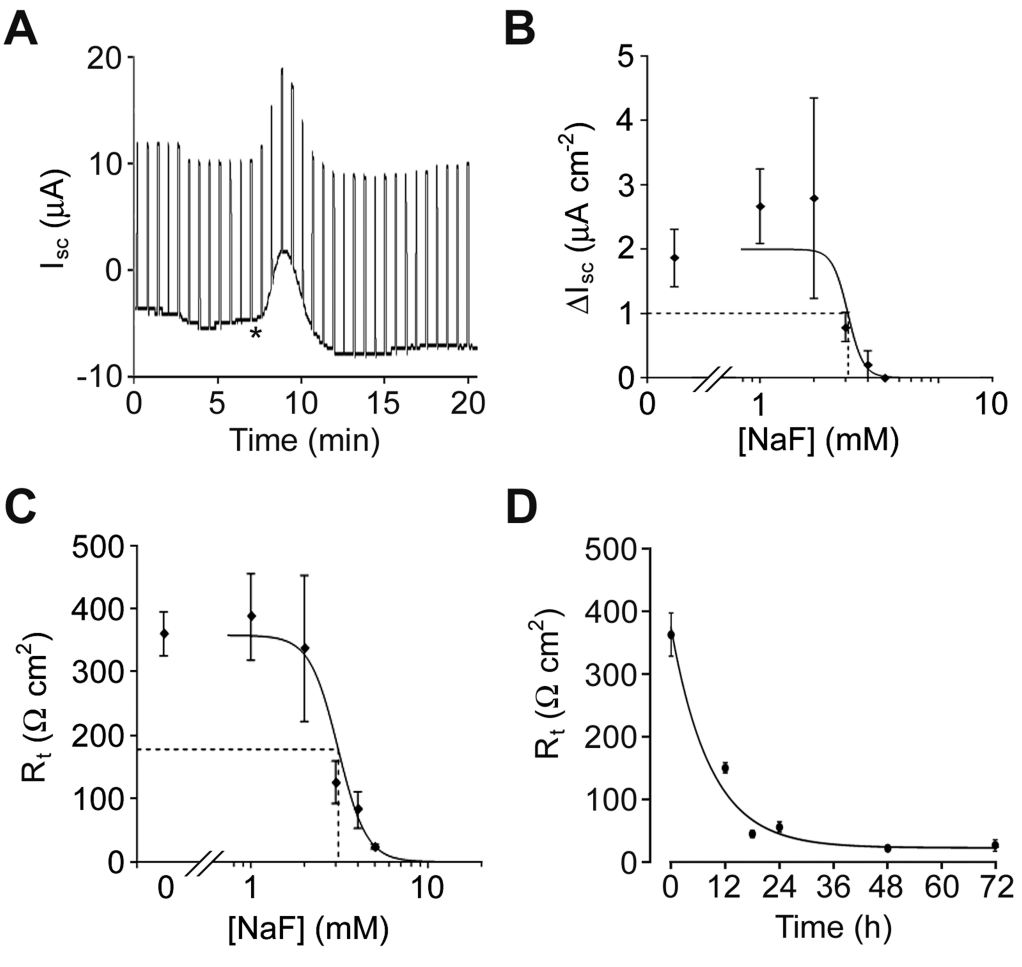
A
20
10
0
-10
I_{sc} (μA)
*
0
5
10
15
20
Time (min)
B
5
4
3
2
1
0
ΔI_{sc} (μA cm^{-2})
0
1
10
[NaF] (mM)
C
500
400
300
200
100
0
R_t (Ω cm^2)
0
1
10
[NaF] (mM)
D
500
400
300
200
100
0
R_t (Ω cm^2)
0
12
24
36
48
60
72
Time (h)

Figure 2

A

Control

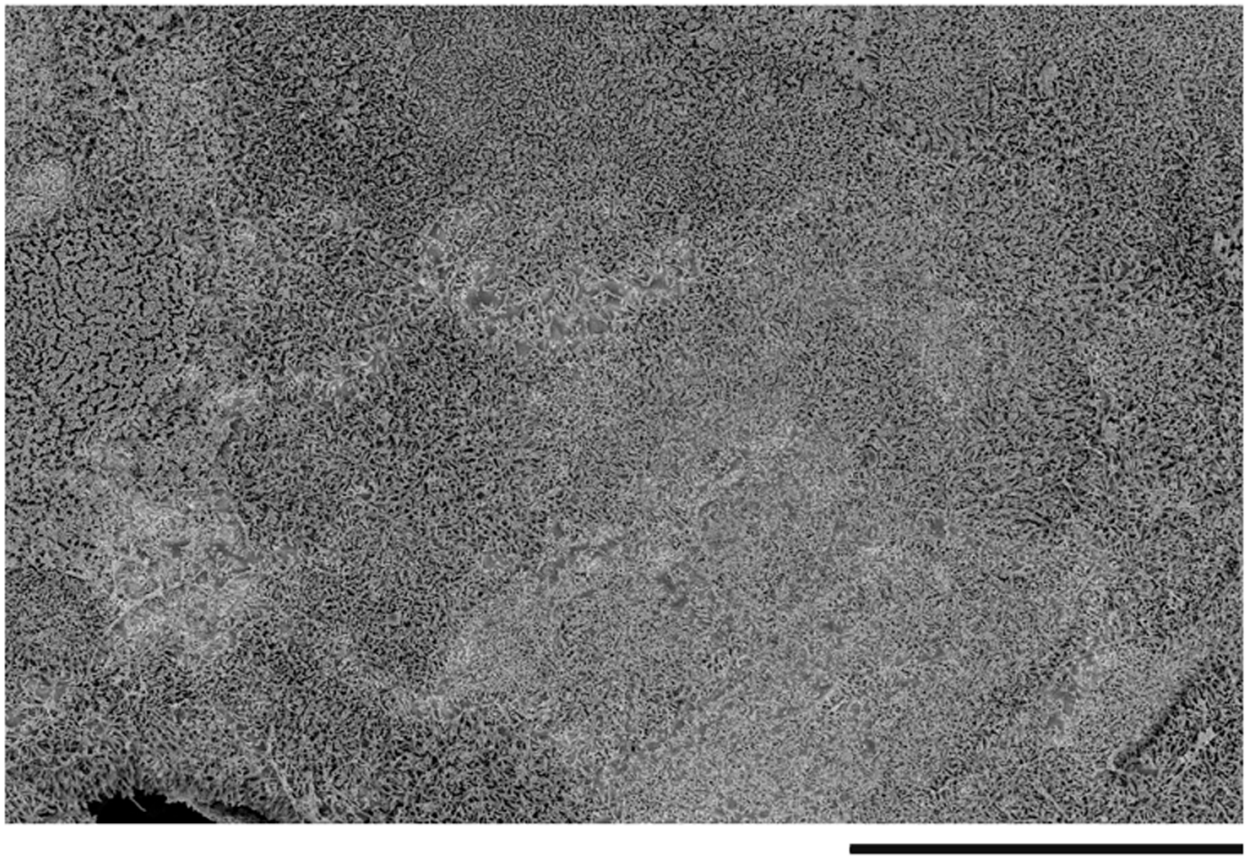

B

5 mM NaF

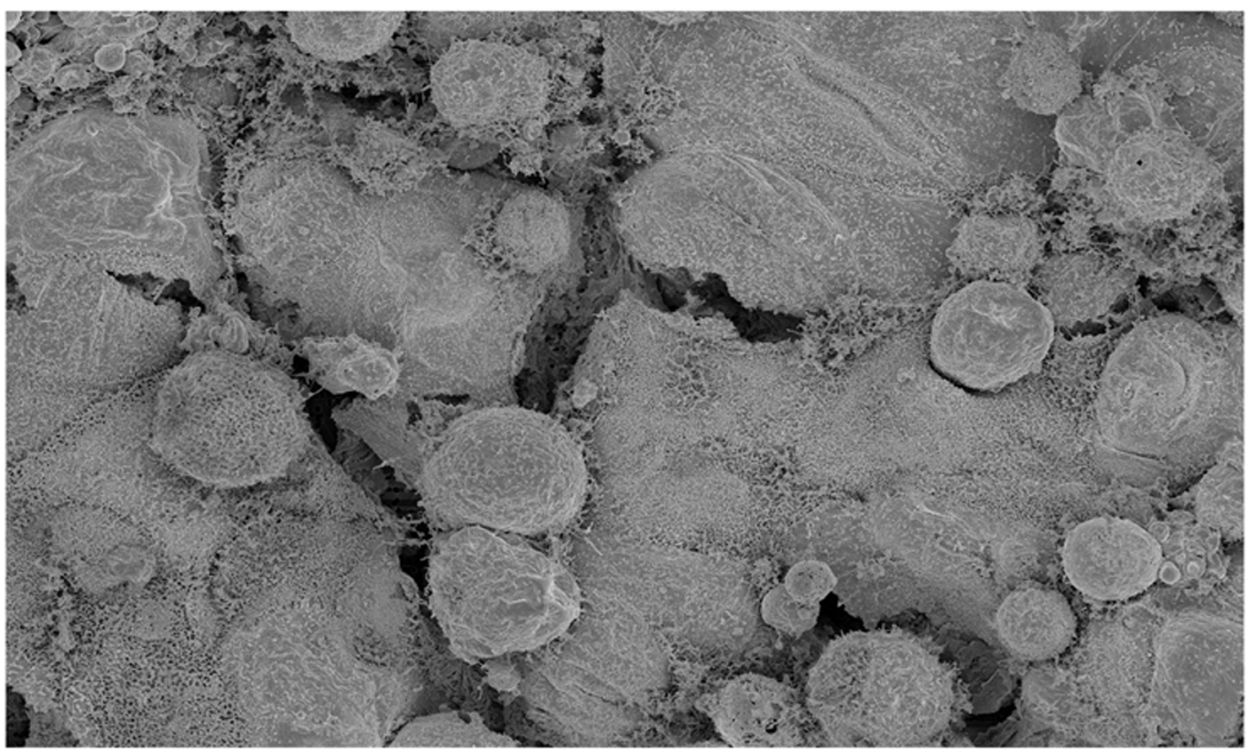

Figure 3

A

Control

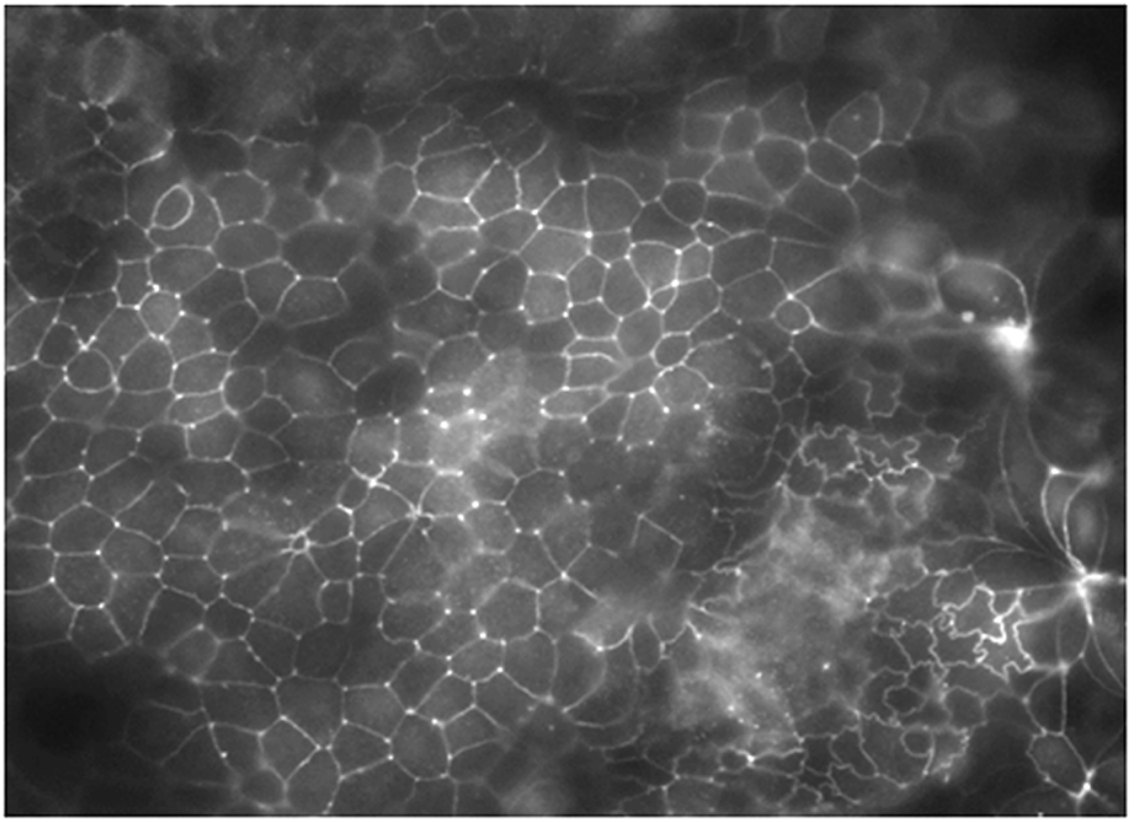

B

5 mM NaF

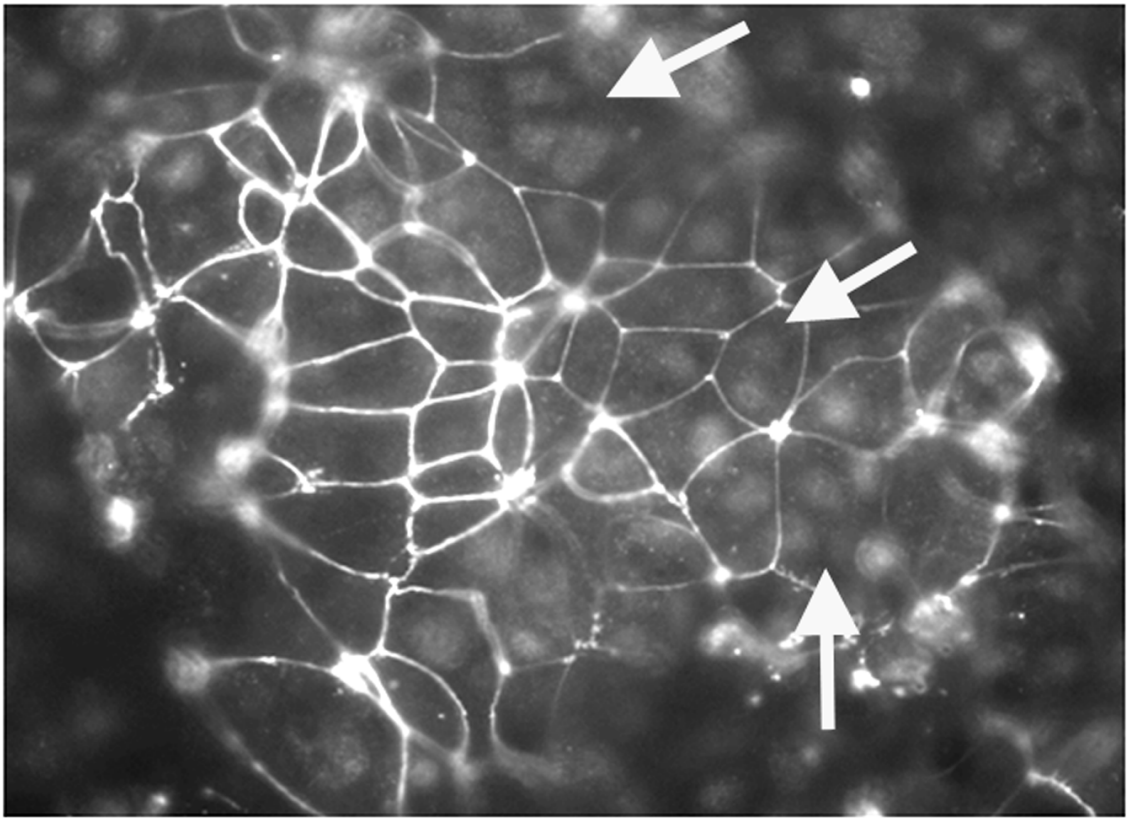

Figure 4

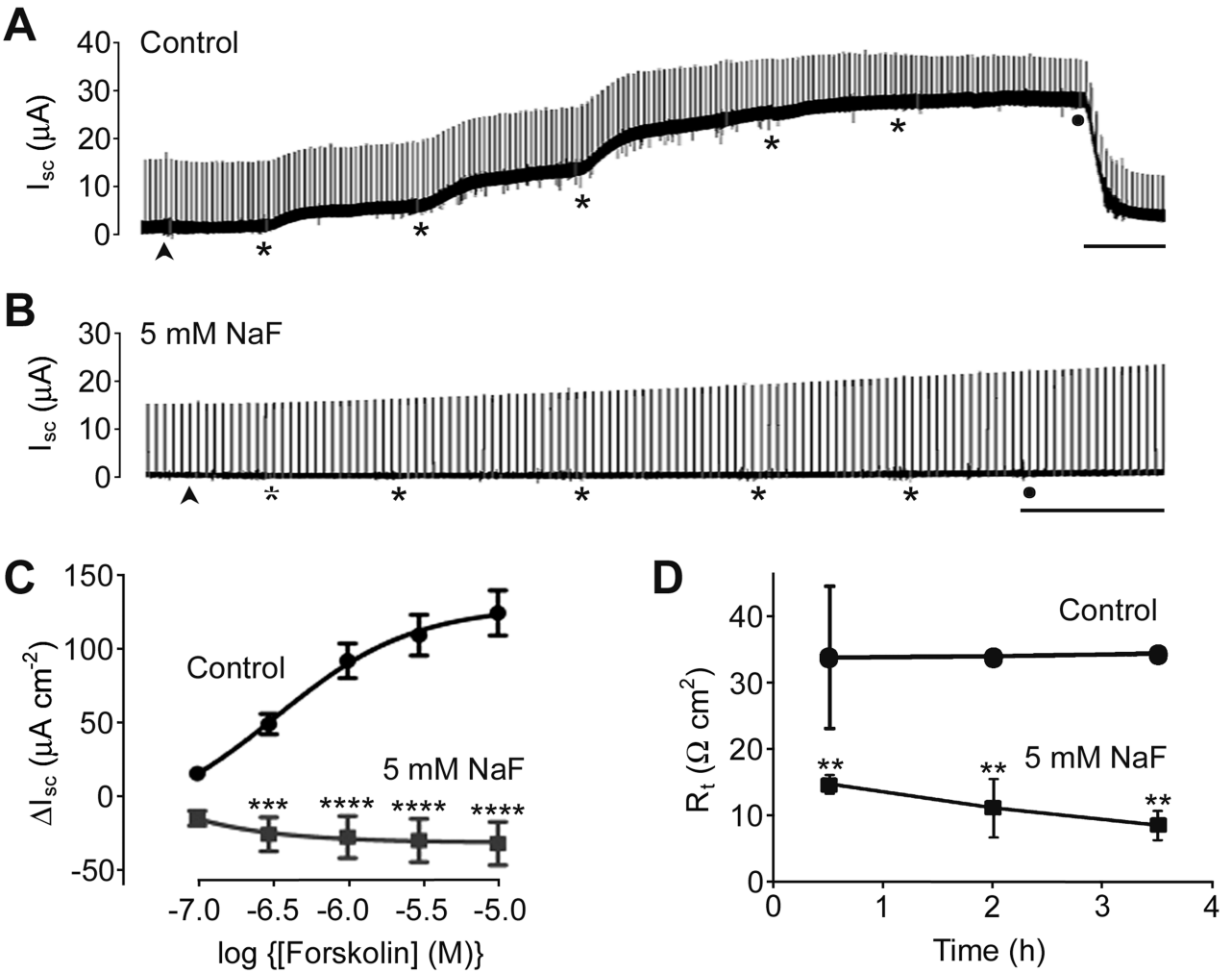
A
Control
I_{sc} (μA)
40
30
20
10
0
B
5 mM NaF
I_{sc} (μA)
30
20
10
0
C
ΔI_{sc} ($\mu A\ cm^{-2}$)
150
100
50
0
-50
Control
5 mM NaF
***
****
****
****
-7.0
-6.5
-6.0
-5.5
-5.0
log {[Forskolin] (M)}
D
R_t ($\Omega\ cm^2$)
40
30
20
10
0
Control
5 mM NaF
**
**
**
0
1
2
3
4
Time (h)

Figure 5

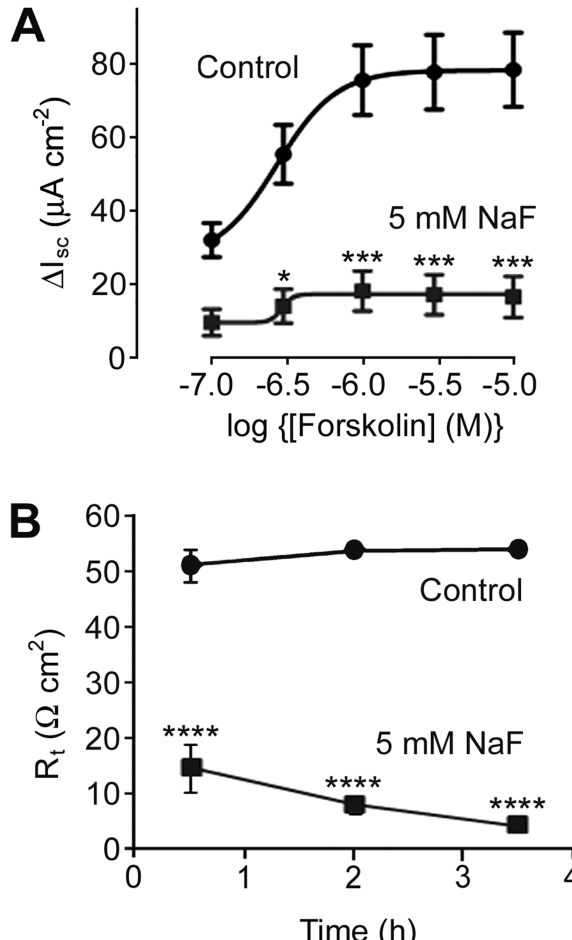
A
Control
5 mM NaF
*
***
***
***
80
60
40
20
0
ΔI_{sc} (μA cm^{-2})
-7.0
-6.5
-6.0
-5.5
-5.0
log {[Forskolin] (M)}
B
Control
5 mM NaF
****
****
****
60
50
40
30
20
10
0
R_t (Ω cm^2)
0
1
2
3
4
Time (h)

Figure 6

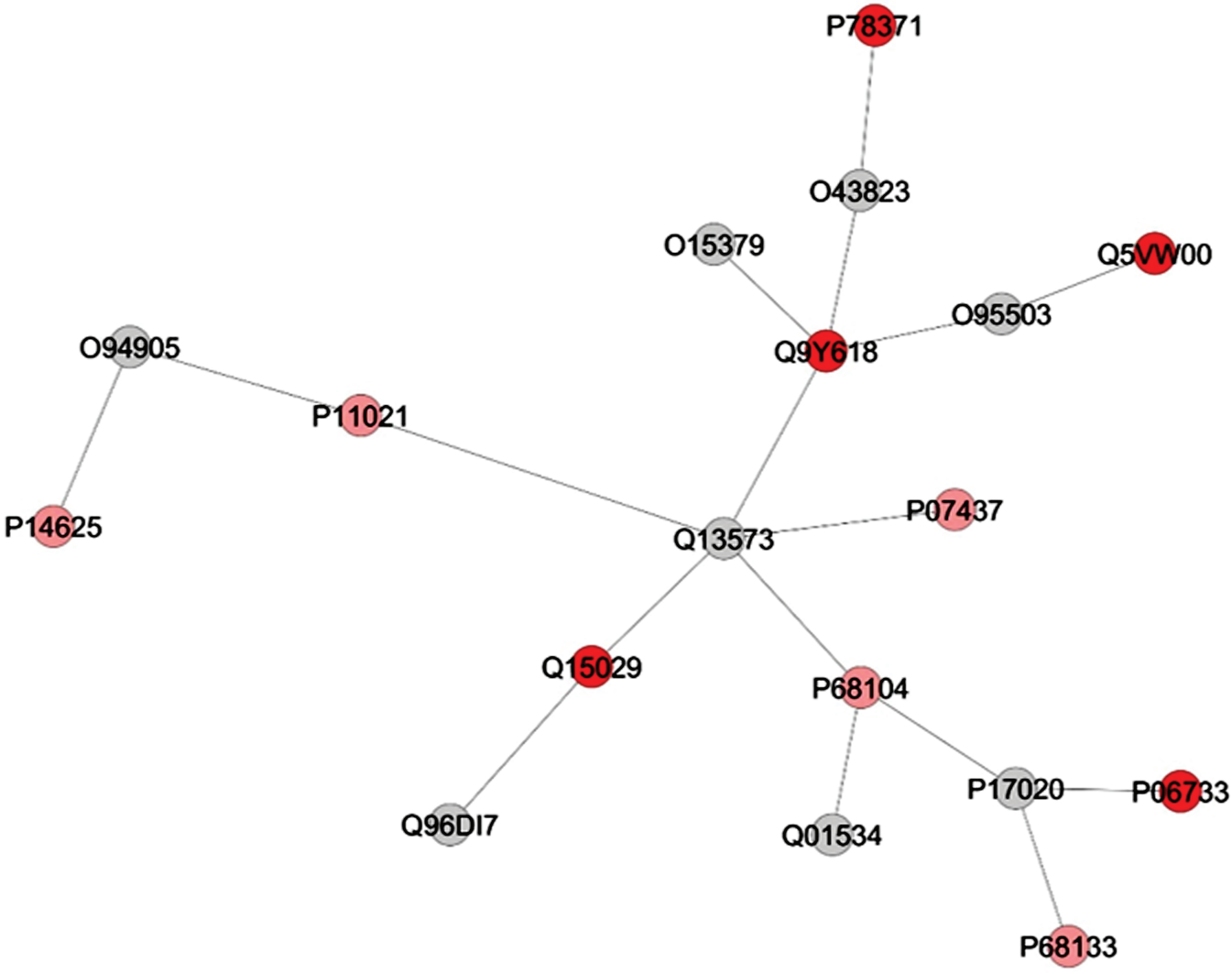
P78371
O43823
O15379
Q5VW00
O95503
Q9Y618
O94905
P11021
P14625
P07437
Q13573
Q15029
P68104
P17020
P06733
Q96DI7
Q01534
P68133

Table SI. Proteins with significant changes in expression in Caco-2 cells treated with 5 mM fluoride compared with control group.

Accession	Gene	Description	PLGS score	Ratio (F:control)
H7C5W8	ACTN1	Alpha-actinin-1 (Fragment)	139.78	3.71
P06748	NPM1	Nucleophosmin	214.84	1.65
O43707	ACTN4	Alpha-actinin-4	160.85	1.40
P12814	ACTN1	Alpha-actinin-1	155.07	1.36
P05787	KRT8	Keratin. type II cytoskeletal 8	102.01	1.16
E9PNX1	SERPINH1	Serpin H1 (Fragment)	302.27	0.94
P06576	ATP5B	ATP synthase subunit beta, mitochondrial	294.93	0.73
P25705	ATP5A1	ATP synthase subunit alpha, mitochondrial	1135.13	0.66
Q14974	KPNB1	Importin subunit beta-1	77.39	0.64
P04350	TUBB4A	Tubulin beta-4A chain	203.76	0.64
D6RBL5	ANXA5	Annexin	129.84	0.63
Q9NY65	TUBA8	Tubulin alpha-8 chain	75.7	0.59
Q13748	TUBA3C	Tubulin alpha-3C/D chain	75.7	0.59
Q6PEY2	TUBA3E	Tubulin alpha-3E	97.19	0.59
P68366	TUBA4A	Tubulin alpha-4A chain	75.7	0.59
H3BUX2	CYB5B	Cytochrome b5 type B	290.73	0.58
H7BZJ3	PDIA3	Protein disulfide-isomerase A3 (Fragment)	343.91	0.58
O43169	CYB5B	Cytochrome b5 type B	290.73	0.58
Q71U36	TUBA1A	Tubulin alpha-1A chain	5341.14	0.58
D6RFH4	CYB5B	Cytochrome b5 type B	290.73	0.58
Q9BQE3	TUBA1C	Tubulin alpha-1C chain	5341.14	0.58
P08758	ANXA5	Annexin A5	347.24	0.58
E9PHT9	ANXA5	Annexin	315.4	0.57
P68363	TUBA1B	Tubulin alpha-1B chain	5341.14	0.57
P14625	HSP90B1	Endoplasmin	324.98	0.54
J3KNF8	CYB5B	Cytochrome b5 type B	290.73	0.54
A0A087X2E9	GSTP1	Glutathione S-transferase P (Fragment)	600.61	0.54

P10809	HSPD1	60 kDa heat shock protein, mitochondrial	1750.41	0.53
Q15084	PDIA6	Protein disulfide-isomerase A6	101.95	0.53
P07900	HSP90AA1	Heat shock protein HSP 90-alpha	551.7	0.52
P0C221	CCDC175	Coiled-coil domain-containing protein 175	75.97	0.52
O00299	CLIC1	Chloride intracellular channel protein 1	210.21	0.51
A8K7Q2	HSPA8	Heat shock cognate 71 kDa protein	203.82	0.51
Q58FF7	HSP90AB3P	Putative heat shock protein HSP 90-beta-3	43.05	0.51
P32119	PRDX2	Peroxiredoxin-2	507.16	0.51
P08238	HSP90AB1	Heat shock protein HSP 90-beta	147.59	0.50
Q06830	PRDX1	Peroxiredoxin-1	507.16	0.50
P40926	MDH2	Malate dehydrogenase. mitochondrial	407.79	0.49
P30101	PDIA3	Protein disulfide-isomerase A3	162.74	0.49
Q96GW1	HSP90B1	Endoplasmin	67.13	0.48
P11142	HSPA8	Heat shock cognate 71 kDa protein	1813.21	0.48
P30084	ECHS1	Enoyl-CoA hydratase. mitochondrial	236.87	0.47
A0A087WVQ9	EEF1A1	Elongation factor 1-alpha 1	515.19	0.46
A0A0G2JIW1	HSPA1B	Heat shock 70 kDa protein 1B	1752.97	0.46
P0DMV9	HSPA1B	Heat shock 70 kDa protein 1B	1752.97	0.46
P68104	EEF1A1	Elongation factor 1-alpha 1	515.19	0.46
Q5VTE0	EEF1A1P5	Putative elongation factor 1-alpha-like 3	515.19	0.46
P0DMV8	HSPA1A	Heat shock 70 kDa protein 1A	1752.97	0.45
E9PNE6	HSPA8	Heat shock cognate 71 kDa protein	1700.33	0.45
J3KPS3	ALDOA	Fructose-bisphosphate	355.5	0.45
E9PKE3	HSPA8	Heat shock cognate 71 kDa protein	1785.87	0.44
P04075	ALDOA	Fructose-bisphosphate aldolase A	355.5	0.44
P12277	CKB	Creatine kinase B-type	212.43	0.44
A8MX94	GSTP1	Glutathione S-transferase P	963.37	0.44
P17066	HSPA6	Heat shock 70 kDa protein 6	1425.92	0.44
G3V3R4	TUBB3	HCG1983504. isoform CRA_c	320.37	0.44
P11021	HSPA5	78 kDa glucose-regulated protein	415.61	0.44
P54652	HSPA2	Heat shock-related 70 kDa protein 2	1774.68	0.44

G3V2R8	TUBB3	HCG1983504, isoform CRA_e	320.37	0.44
G3V5W4	TUBB3	Tubulin beta-3 chain	320.37	0.44
P09211	GSTP1	Glutathione S-transferase P	963.37	0.44
G3V2N6	TUBB3	HCG1983504. isoform CRA_d	320.37	0.44
Q05639	EEF1A2	Elongation factor 1-alpha 2	95.38	0.43
P62937	PPIA	Peptidyl-prolyl cis-trans isomerase A	1440.16	0.43
P60709	ACTB	Actin, cytoplasmic 1	575.04	0.43
F5H5D3	TUBA1C	Tubulin alpha-1C chain	5341.14	0.43
P63261	ACTG1	Actin, cytoplasmic 2	575.04	0.43
Q9BYX7	POTEKP	Putative beta-actin-like protein 3	502.31	0.42
A5A3E0	POTEKP	POTE ankyrin domain family member F	502.31	0.42
F8WE65	PPIA	Peptidyl-prolyl cis-trans isomerase	1440.16	0.42
Q13885	TUBB2A	Tubulin beta-2A chain	1454.28	0.42
P34931	HSPA1L	Heat shock 70 kDa protein 1-like	1786.52	0.42
P38646	HSPA9	Stress-70 protein, mitochondrial	854.97	0.42
Q9BVA1	TUBB2B	Tubulin beta-2B chain	1454.28	0.42
Q562R1	ACTBL2	Beta-actin-like protein 2	507.48	0.42
P63267	ACTG2	Actin, gamma-enteric smooth muscle	507.48	0.42
Q6S8J3	POTEE	POTE ankyrin domain family member E	502.31	0.42
Q13509	TUBB3	Tubulin beta-3 chain	1443.49	0.41
P48741	HSPA7	Putative heat shock 70 kDa protein 7	1404.53	0.41
P00558	PGK1	Phosphoglycerate kinase 1	119.27	0.41
A0A0B4J269		Uncharacterized protein	1443.49	0.41
F8VS66	TUBA1C	Tubulin alpha-1C chain	5265.44	0.41
Q5JP53	TUBB	Tubulin beta chain	1454.28	0.41
V9GZ37	HSPA1A	Heat shock 70 kDa protein 1A	81.96	0.41
P68133	ACTA1	Actin, alpha skeletal muscle	507.48	0.41
P07437	TUBB	Tubulin beta chain	1454.28	0.41
P68032	ACTC1	Actin, alpha cardiac muscle 1	507.48	0.41
P62736	ACTA2	Actin, aortic smooth muscle	507.48	0.41
P13796	LCP1	Plastin-2	48.98	0.41

H3BQN4	ALDOA	Fructose-bisphosphate aldolase	355.5	0.41
G3V2A3	TUBB3	Tubulin beta-3 chain (Fragment)	1123.12	0.41
A0A087WUM2	LDHAL6A	L-lactate dehydrogenase	80.83	0.40
Q5ST81	TUBB	Tubulin beta chain	1133.91	0.40
P68371	TUBB4B	Tubulin beta-4B chain	1326.88	0.40
P55072	VCP	Transitional endoplasmic reticulum ATPase	68.43	0.40
P30041	PRDX6	Peroxiredoxin-6	236.73	0.39
O60486	PLXNC1	Plexin-C1	17.18	0.39
P00338	LDHA	L-lactate dehydrogenase A chain	80.83	0.38
Q6ZMR3	LDHAL6A	L-lactate dehydrogenase A-like 6A	85.76	0.38
Q3ZCM7	TUBB8	Tubulin beta-8 chain	203.76	0.38
A0A075B724	TUBB8	Tubulin beta-8 chain	192.97	0.37
P09104	ENO2	Gamma-enolase	101.14	0.37
M0QX14	TUBB4A	Tubulin beta-4A chain	192.97	0.37
P07195	LDHB	L-lactate dehydrogenase B chain	120.82	0.36
P0CG39	POTEJ	POTE ankyrin domain family member J	293.29	0.29
P0CG38	POTEI	POTE ankyrin domain family member I	286.08	0.29
E5RIZ5	PPIA	Peptidyl-prolyl cis-trans isomerase A	731.15	0.27
C9J5S7	PPIA	Peptidyl-prolyl cis-trans isomerase	1440.16	0.26

Identified proteins are organized according to the PLGS score. Identification is based on protein ID from UniProt protein database (http://www.uniprot.org/).

Table SII. Proteins identified exclusively in untreated Caco-2 cells (control).

Accession	Gene	Description	PLGS score
P31939	ATIC	Bifunctional purine biosynthesis protein PURH	604.69
D6R904	TPM3	Tropomyosin alpha-3 chain	426.32
Q5HYB6	DKFZp686J1372	Epididymis luminal protein 189	426.32
Q8NA19	L3MBTL4	Lethal(3)malignant brain tumor-like protein 4	397.51
P13639	EEF2	Elongation factor 2	326.82
Q15029	EFTUD2	116 kDa U5 small nuclear ribonucleoprotein component	307.44
P06733	ENO1	Alpha-enolase	252.36
E5RGE1	YWHAZ	14-3-3 protein zeta/delta (Fragment)	251.38
H3BRD5	MYO9A	Unconventional myosin-IXa	248.17
B2RTY4	MYO9A	Unconventional myosin-IXa	248.17
Q5VU61	TPM3	Tropomyosin alpha-3 chain	240.83
K7EL95	QTRT1	Queuine tRNA-ribosyltransferase (Fragment)	240.33
J3KQ43	ALS2	Alsin (Fragment)	230.18
H0Y8Y2	ANK2	Ankyrin-2 (Fragment)	225.34
Q9BWD1	ACAT2	Acetyl-CoA acetyltransferase. cytosolic	219.28
H7BYH4	SOD1	Superoxide dismutase [Cu-Zn]	216.39
Q58EX7	PLEKHG4	Puratrophin-1	215.35
H3BR70	PKM	Pyruvate kinase	215.17
P35579	MYH	Myosin-9	214.35
H3BQP9	PLEKHG4	Puratrophin-1 (Fragment)	212.05
H0Y933	ANK2	Ankyrin-2 (Fragment)	202.89
B1AH99	MYH9	Myosin-9 (Fragment)	200.43
Q5BKV1	MYH9	MYH9 protein	200.43
P18206	VCL	Vinculin	187.78
H0YK48	TPM1	Tropomyosin alpha-1 chain	185.49
J3KN67	TPM3	Tropomyosin alpha-3 chain	185.49
P13797	PLS3	Plastin-3	182.39
F5H0C5	PHB2	Prohibitin-2	180.6
X6R3G6	MFGE8	Lactadherin	174.75
P15822	HIVEP1	Zinc finger protein 40	171.73
I3L504	EIF5A	Eukaryotic translation initiation factor 5A-1	171.23
O95994	AGR2	Anterior gradient protein 2 homolog	169.8
A0A0A0MSQ0	PLS3	Plastin-3	168.48
F5H212	HIVEP1	Zinc finger protein 40	168.17
Q9UKA1	FBXL5	F-box/LRR-repeat protein 5	165.83
Q9HC52	CBX8	Chromobox protein homolog 8	159.88
H7C0P3	NCOR2	Nuclear receptor corepressor 2 (Fragment)	159.79
A0A096LPE1	VCL	Vinculin	159.5
P07864	LDHC	L-lactate dehydrogenase C chain	159.42
F5H245	LDHC	L-lactate dehydrogenase	159.42
Q9UBB9	TFIP11	Tuftelin-interacting protein 11	157.39

C9J2N3	HIVEP1	Zinc finger protein 40 (Fragment)	157.15
Q16586	SGCA	Alpha-sarcoglycan	148.07
Q9UGJ1	TUBGCP4	Gamma-tubulin complex component 4	140.96
F5H365	SEC23A	Protein transport protein Sec23A	140.63
F8W775	NRCAM	Neuronal cell adhesion molecule	137.15
H3BQY4	TUBGCP4	Gamma-tubulin complex component 4 (Fragment)	131.05
A0A087X2B3	NRCAM	Neuronal cell adhesion molecule	130.06
Q9NUJ7	PLCXD1	PI-PLC X domain-containing protein 1	129.95
C9JP92	PLCXD1	PI-PLC X domain-containing protein 1 (Fragment)	129.95
X6RFG1	PLCXD1	PI-PLC X domain-containing protein 1 (Fragment)	129.95
Q9BXI2	SLC25A2	Mitochondrial ornithine transporter 2	127.87
Q9UN70	PCDHGC3	Protocadherin gamma-C3	123.77
G3V5X8	SEC23A	Protein transport protein Sec23A	121.08
Q9Y5F6	PCDHGC5	Protocadherin gamma-C5	118.22
F5GXQ8	SYNE1	Nesprin-1	117.96
P35243	RCVRN	Recoverin	116.92
Q7Z3Z4	PIWIL4	Piwi-like protein 4	116.87
Q5VW00	DCAF12L2	DDB1- and CUL4-associated factor 12-like protein 2	115.37
Q03403	TFF2	Trefoil factor 2	115.28
Q9Y5H1	PCDHGA2	Protocadherin gamma-A2	114.39
P68036	UBE2L3	Ubiquitin-conjugating enzyme E2 L3	113.46
A6NIW5	PRDX2	Peroxiredoxin 2, isoform CRA_a	111.75
A0A0A0MRI2	SNX6	Sorting nexin 6, isoform CRA_b	111.38
Q9UNH7	SNX6	Sorting nexin-6	111.38
Q9Y5G2	PCDHGB2	Protocadherin gamma-B2	111.32
Q16854	DGUOK	Deoxyguanosine kinase. mitochondrial	110.51
A0A0A0MQW1	KSR1	Protein kinase C	110.47
Q8IVT5	KSR1	Kinase suppressor of Ras 1	110.47
O00764	PDXK	Pyridoxal kinase	110.18
P98160	HSPG2	Basement membrane-specific heparan sulfate proteoglycan core protein	108.94
Q9Y5G1	PCDHGB3	Protocadherin gamma-B3	108.32
Q6WCQ1	MPRIP	Myosin phosphatase Rho-interacting protein	106.18
H0YMU7	KMT2C	Histone-lysine N-methyltransferase 2C	105.6
P18615	NELFE	Negative elongation factor E	105.31
F5H422	SYNE1	Nesprin-1	103.79
Q13315	ATM	Serine-protein kinase ATM	103.62
F5H4Q0	SYNE1	Nesprin-1	101.21
Q8WV37	ZNF480	Zinc finger protein 480	99.51
Q9Y5G3	PCDHGB	Protocadherin gamma-B1	99.11
Q9Y5G0	PCDHGB5	Protocadherin gamma-B5	99.11
A0A0U1RQT3	HSPG2	Basement membrane-specific heparan sulfate proteoglycan core protein (Fragment)	99.11
Q9BQI5	SGIP1	SH3-containing GRB2-like protein 3-interacting protein 1	98.31
O00567	NOP56	Nucleolar protein 56	97.79
A0A087WUC2	PCDHGC4	Protocadherin gamma-C4	97.17
Q9Y5H4	PCDHGA1	Protocadherin gamma-A1	97.17

Q9Y5H3	PCDHGA10	Protocadherin gamma-A10	97.17
Q9Y5H2	PCDHGA11	Protocadherin gamma-A11	97.17
Q9Y5H0	PCDHGA3	Protocadherin gamma-A3	97.17
Q9Y5G9	PCDHGA4	Protocadherin gamma-A4	97.17
Q9Y5G8	PCDHGA5	Protocadherin gamma-A5	97.17
Q9Y5G7	PCDHGA6	Protocadherin gamma-A6	97.17
Q9Y5G6	PCDHGA7	Protocadherin gamma-A7	97.17
Q9Y5G5	PCDHGA8	Protocadherin gamma-A8	97.17
Q9Y5G4	PCDHGA9	Protocadherin gamma-A9	97.17
Q9Y5F9	PCDHGB6	Protocadherin gamma-B6	97.17
Q9Y5F8	PCDHGB7	Protocadherin gamma-B7	97.17
Q9Y5F7	PCDHGC4	Protocadherin gamma-C4	97.17
Q9UN71	PCDHGB4	Protocadherin gamma-B4	97.17
Q9BR81	PCDHGC3	Protocadherin gamma subfamily C. 3	97.17
A0A087WT05	PCDHGA4	Protocadherin gamma-A4	97.17
A0A087WYB5	PCDHGC3	Protocadherin gamma-C3	97.17
O60330	PCDHGA12	Protocadherin gamma-A12	97.17
P78371	CCT2	T-complex protein 1 subunit beta	97.14
F5GWF6	CCT2	T-complex protein 1 subunit beta	97.14
B9A041	MDH1	Malate dehydrogenase. cytoplasmic	95.61
Q9BSH5	HDHD3	Haloacid dehalogenase-like hydrolase domain-containing protein 3	94.33
Q8IXJ6	SIRT2	NAD-dependent protein deacetylase sirtuin-2	94.13
D6REN3	PSMG4	Proteasome assembly chaperone 4	93.54
F5H116	PIWIL4	Piwi-like protein 4	91.82
E9PD43	NELFE	Negative elongation factor E (Fragment)	91.39
G3V2U1	SNX6	Sorting nexin-6	91.38
Q8TEW0	PARD3	Partitioning defective 3 homolog	91.36
F6R8P8	SGIP1	SH3-containing GRB2-like protein 3-interacting protein 1 (Fragment)	91.1
H7C5N6	ASIC3	Acid-sensing ion channel 3 (Fragment)	90.61
H0YFT4	SYNE1	Nesprin-1 (Fragment)	90.51
F8W1K6	PLXNC1	Plexin-C1	90.23
H0YHE0	HEATR5A	HEAT repeat-containing protein 5A (Fragment)	89.68
P35613	BSG	Basigin	88.52
P38159	RBMX	RNA-binding motif protein, X chromosome	88.05
E7EUT5	GAPDH	Glyceraldehyde-3-phosphate dehydrogenase	87.3
Q5VWU8	PARD3	Partitioning defective 3 homolog	86.75
E9PCA1	CCT5	T-complex protein 1 subunit epsilon	85.59
P51689	ARSD	Arylsulfatase D	84.67
H0Y7E2	MPRIP	Myosin phosphatase Rho-interacting protein (Fragment)	84.4
Q5VWV2	PARD3	Partitioning defective 3 homolog	83.94
P09622	DLD	Dihydrolipoyl dehydrogenase. mitochondrial	82.64
Q92954	PRG4	Proteoglycan 4	82.36
O43615	TIMM44	Mitochondrial import inner membrane translocase subunit TIM44	81.79
G3V140	CEP57L1	Centrosomal protein CEP57L1	81.68
Q6P2R3	C6orf182	C6orf182 protein	81.68

F5GZI3	PARD3	Partitioning defective 3 homolog	79.32
A0A0A0MT41	PLCXD1	PI-PLC X domain-containing protein 1 (Fragment)	78.85
Q9H841	NIPAL2	NIPA-like protein 2	78.79
E9PEX6	DLD	Dihydrolipoyl dehydrogenase	78.72
Q86UP8	GTF2IRD2	General transcription factor II-I repeat domain-containing protein 2A	78.57
Q6EKJ0	GTF2IRD2B	General transcription factor II-I repeat domain-containing protein 2B	78.57
E5RJN3	NCAPH2	Condensin-2 complex subunit H2 (Fragment)	78.19
H7C327	ARSD	Arylsulfatase D (Fragment)	77.96
Q5QPM2	RALY	RNA-binding protein Raly (Fragment)	75.39
Q9Y618	NCOR2	Nuclear receptor corepressor 2	74.87
G5E977	NAPRT	Nicotinate phosphoribosyltransferase	74.87
P41970	ELK3	ETS domain-containing protein Elk-3	74.61
Q6IQ55	TTBK2	Tau-tubulin kinase 2	73.66
Q5GLZ8	HERC4	Probable E3 ubiquitin-protein ligase HERC4	72.95
H3BUY5	RBMX	RNA-binding motif protein. X chromosome	72.77
Q8N4C6	NIN	Ninein	72.6
Q5JXT2	NOP56	Nucleolar protein 56 (Fragment)	72.13
B1AP52	PARD3	Partitioning defective 3 homolog	72
J3QRL2	MPRIP	Myosin phosphatase Rho-interacting protein (Fragment)	71.82
H0Y8T1	SGCA	Alpha-sarcoglycan (Fragment)	71.68
P14866	HNRNPL	Heterogeneous nuclear ribonucleoprotein L	70.48
C9J066	NIN	Ninein	69.31
M0R2S2	EPS15L1	Epidermal growth factor receptor substrate 15-like 1	69.07
H0Y6K7	HERC4	Probable E3 ubiquitin-protein ligase HERC4 (Fragment)	69.02
Q13439	GOLGA4	Golgin subfamily A member 4	68.25
A6ZIE4	MUC1	MUC1 isoform M10	67.94
A6ZIE3	MUC1	MUC1 isoform M9	67.94
B1AVQ7	MUC1	Mucin-1	67.94
F8WCH0	ACTG2	Actin, gamma-enteric smooth muscle	67.19
G5E9R0	ACTB	Actin, cytoplasmic 1	67.19
F8WB63	ACTG2	Actin, gamma-enteric smooth muscle	67.19
J3KT65	ACTG1	Actin, cytoplasmic 2	67.19
Q9UIJ7	AK3	GTP:AMP phosphotransferase AK3, mitochondrial	67.19
H0YM25	GOLGA6L22	Golgin subfamily A member 6-like protein 22	66.77
O95271	TNKS	Tankyrase-1	65.89
F8VQ14	CCT2	T-complex protein 1 subunit beta	64.31
P21549	AGXT	Serine--pyruvate aminotransferase	63.53
Q8IZA0	KIAA0319L	Dyslexia-associated protein KIAA0319-like protein	63.22
O95613	PCNT	Pericentrin	63.06
Q12765	SCRN1	Secernin-1	62.31
O00192	ARVCF	Armadillo repeat protein deleted in velo-cardio-facial syndrome	62.23
E7EWY6	TNKS	Tankyrase-1	62.2
A0A0B4J292	TTBK2	Tau-tubulin kinase 2	61.74
Q8TD31	CCHCR1	Coiled-coil alpha-helical rod protein	60.29
B1AN15	KIAA0319L	Dyslexia-associated protein KIAA0319-like protein (Fragment)	60.1

B4DYG9	KIAA0319L	Dyslexia-associated protein KIAA0319-like protein	60.1
H0YDE5	KIAA1549L	UPF0606 protein KIAA1549L (Fragment)	59.92
H0YME6	KIF23	Kinesin-like protein	59.34
Q17RN3	FAM98C	Protein FAM98C	59.15
P30520	ADSS	Adenylosuccinate synthetase isozyme 2	59.08
K7EQV0	NLRP11	NACHT, LRR and PYD domains-containing protein 11	58.44
Q8N7Z2	GOLGA6L1	Golgin subfamily A member 6-like protein 1	58.06
A8MZA4	GOLGA6L6	Golgin subfamily A member 6-like protein 6	58.06
P08243	ASNS	Asparagine synthetase [glutamine-hydrolyzing]	57.22
B8ZZP4	SCRN1	Secernin-1	56.35
C9JJX6	ARVCF	Armadillo repeat protein deleted in velo-cardio-facial syndrome	55.95
Q9BW61	DDA1	DET1- and DDB1-associated protein 1	55.36
P54278	PMS2	Mismatch repair endonuclease PMS2	55.27
Q14232	EIF2B1	Translation initiation factor eIF-2B subunit alpha	55.26
P10632	CYP2C8	Cytochrome P450 2C8	55.16
P24821	TNC	Tenascin	54.66
Q9H4A4	RNPEP	Aminopeptidase B	54.59
O15049	N4BP3	NEDD4-binding protein 3	53.76
H3BS38	GOLGA6L2	Golgin subfamily A member 6-like protein 2	53.21
Q53F39	MPPE1	Metallophosphoesterase 1	53.21
Q58FF6	HSP90AB4P	Putative heat shock protein HSP 90-beta 4	52.77
Q9UPN4	CEP131	Centrosomal protein of 131 kDa	52.42
Q5TZA2	CROCC	Rootletin	51.91
A6NKB8	RNPEP	Aminopeptidase B	51.22
C9JHJ5	GOLGA4	Golgin subfamily A member 4 (Fragment)	50.95
A0A0B4J1R6	TKT	Transketolase	48.8
P29401	TKT	Transketolase	48.8
K7EJ21	QTRT1	Queuine tRNA-ribosyltransferase (Fragment)	48.36
K7ESP6	QTRT1	Queuine tRNA-ribosyltransferase (Fragment)	48.36
I3L2X7	CEP131	Centrosomal protein of 131 kDa (Fragment)	45.01
P46108	CRK	Adapter molecule crk	43.67
Q00341	HDLBP	Vigilin	41.77
A0A0A0MRF5	SIRT2	NAD-dependent protein deacetylase sirtuin-2	39.73
A0A087WYM3	SIRT2	NAD-dependent protein deacetylase sirtuin-2	39.73
E7EWX6	SIRT2	NAD-dependent protein deacetylase sirtuin-2 (Fragment)	39.73
H0Y394	HDLBP	Vigilin (Fragment)	39.71
A0A024R4E5	HDLBP	High density lipoprotein binding protein (Vigilin). isoform CRA_a	39.71
I3L2J8	CEP131	Centrosomal protein of 131 kDa	39.32
Q14145	KEAP1	Kelch-like ECH-associated protein 1	34.64
A0A0G2JP78	RAD17	Cell cycle checkpoint protein RAD17	32.34
O75943	RAD17	Cell cycle checkpoint protein RAD17	32.34
A0A0G2JPT5	RAD17	Cell cycle checkpoint protein RAD17	32.34
Q13127	REST	RE1-silencing transcription factor	32.15
Q01484	ANK2	Ankyrin-2	31.91
Q3V6T2	CCDC88A	Girdin	31.6

E9PEI6	DPCR1	Diffuse panbronchiolitis critical region protein 1	26.7
I6L894	ANK2	Ankyrin-2	26.1
O75643	SNRNP200	U5 small nuclear ribonucleoprotein 200 kDa helicase	25.7
A4UGR9	XIRP2	Xin actin-binding repeat-containing protein 2	24.44
Q5HYC2	KIAA2026	Uncharacterized protein KIAA2026	24.2
H0Y786	NEB	Nebulin (Fragment)	18.28
H0YEM4	VWA3B	von Willebrand factor A domain-containing protein 3B (Fragment)	18
Q9P2D7	DNAH1	Dynein heavy chain 1. axonemal	17.05

Identified proteins are organized according to the PLGS score. Identification is based on protein ID from UniProt protein database (http://www.uniprot.org/).

Table SIII. Proteins identified exclusively in fluoride-treated Caco-2 cells.

Accession	Gene	Description	PLGS score
H0YMU9	ANXA2	Annexin	1593.78
P07355	ANXA2	Annexin A2	1593.78
E5RGW4	NPM1	Nucleophosmin (Fragment)	250.85
J3KSH9	ITGB4	Integrin beta-4 (Fragment	247.77
A0A0C4DGS6	BCAS4	Breast carcinoma-amplified sequence	237.43
Q8TDM0	BCAS4	Breast carcinoma-amplified sequence 4	237.43
A0A0U1RQV5	uncharacterized	Uncharacterized protein (Fragment)	214.16
Q5JYR7	RPN2	Dolichyl-diphosphooligosaccharide--protein glycosyltransferase subunit 2 (Fragment)	193.9
Q5JYR4	RPN2	Dolichyl-diphosphooligosaccharide--protein glycosyltransferase subunit 2 (Fragment)	193.9
P04844	RPN2	Dolichyl-diphosphooligosaccharide--protein glycosyltransferase subunit 2	193.9
W4VSR2	MPND	MPN domain-containing protein	181.72
H0YJ09	HAUS4	HAUS augmin-like complex subunit 4 (Fragment)	181.55
Q9P253	VPS18	Vacuolar protein sorting-associated protein 18 homolog	172.92
P13929	ENO3	Beta-enolase	172.1
H0YMC9	VPS18	Vacuolar protein sorting-associated protein 18 homolog	164.5
J3KTM9	KPNB1	Importin subunit beta-1 (Fragment	160.11
J3QRG4	KPNB1	Importin subunit beta-1 (Fragment)	158.13
F8VY02	ERP29	Endoplasmic reticulum resident protein 29	143.29
P30040	ERP29	Endoplasmic reticulum resident protein 29	143.29
F5H0C8	ENO2	Enolase	138.07
F8VUW4	PLXNC1	Plexin-C1 (Fragment)	136.15
A6NMY6	ANXA2	Putative annexin A2-like protein	132.54
I3L391	CACNA1A	Voltage-dependent P/Q-type calcium channel subunit alpha-1A (Fragment)	109.81
Q7Z494	NPHP3	Nephrocystin-3	108.79
Q6DKI2	LGALS9C	Galectin-9C	107.29
Q3B8N2	LGALS9B	Galectin-9B	107.29
Q6DN72	FCRL6	Fc receptor-like protein 6	104.59
F5GYB3	FCRL6	Fc receptor-like protein 6 (Fragment)	104.59
Q8N5I4	vPS18	Dehydrogenase/reductase SDR family member on chromosome X	104.37
P51571	SSR4	Translocon-associated protein subunit delta	100.78
A0A0J9YXS1	NPHP3-ACAD11	Protein NPHP3-ACAD11 (Fragment	95.06
A0A0A0MQU4	SCLY	Selenocysteine lyase	88.85
Q96I15	SCLY	Selenocysteine lyase	88.85
E9PFF5	FXR1	Fragile X mental retardation syndrome-related protein 1	87.67
H7C4Y8	BCAS4	Breast carcinoma-amplified sequence 4	87.44
H3BR68	ALDOA	Fructose-bisphosphate aldolase A (Fragment)	87.03
A6NMU3	STAM	Signal transducing adapter molecule 1 (Fragment)	80.12
A1L0T0	ILVBL	Acetolactate synthase-like protein	79.34
P31150	GDI1	Rab GDP dissociation inhibitor alpha	79.19

B4DQB2	VNN2	Vascular non-inflammatory molecule 2	76.89
J3KQQ7	VNN2	Vascular non-inflammatory molecule 2	76.89
J3QT03	VNN2	Vascular non-inflammatory molecule 2	76.89
Q96RU2	USP28	Ubiquitin carboxyl-terminal hydrolase 28	74.97
F5H0E2	SLC3A2	4F2 cell-surface antigen heavy chain (Fragment)	74.53
Q9UHB7	AFF4	AF4/FMR2 family member 4	71.08
F5H8A6	TNFRSF1A	Tumor necrosis factor receptor superfamily member 1A (Fragment)	71.01
P39687	ANP32A	Acidic leucine-rich nuclear phosphoprotein 32 family member A	70.02
Q92688	ANP32B	Acidic leucine-rich nuclear phosphoprotein 32 family member B	70.02
C9JCE0	AFF4	AF4/FMR2 family member 4 (Fragment	68.97
F5GZ74	USP28	Ubiquitin carboxyl-terminal hydrolase 28	66.94
Q86YA3	ZGRF1	Protein ZGRF1	64.56
O95197	RTN3	Reticulon-3	63.86
Q9UHD1	CHORDC1	Cysteine and histidine-rich domain-containing protein 1	63.79
Q8N1H7	SIX6OS1	Protein SIX6OS1	63.53
G3XAL8	ZGRF1	HCG21296, isoform CRA_a	62.92
Q9H6D7	HAUS4	HAUS augmin-like complex subunit 4	60.8
B7Z4M1	RTN3	Reticulon	59.74
Q6ZUS5	CCDC121	Coiled-coil domain-containing protein 121	58.28
P51172	SCNN1D	Amiloride-sensitive sodium channel subunit delta	58.17
J3QR96	LGALS9C	Galectin	57.64
P07237	GN=P4HB	Protein disulfide-isomerase	55.83
P11169	GN=SLC2A3	Solute carrier family 2. facilitated glucose transporter member 3	55.66
O94761	RECQL4	ATP-dependent DNA helicase Q4	55.4
G5E9G6	TRIP12	E3 ubiquitin-protein ligase TRIP12	54.38
E9PS00	FADS3	Fatty acid desaturase 3	52.72
O14772	FPGT	Fucose-1-phosphate guanylyltransferase	50.8
D6REN9	ZGRF1	Protein ZGRF1 (Fragment)	49.88
O00182	LGALS9	Galectin-9	49.65
Q96S94	CCNL2	Cyclin-L2	48.94
F8W876	MASP1	Mannan-binding lectin serine protease 1	48.48
G3V1X1	ZFC3H1	Proline/serine-rich coiled-coil 2. isoform CRA_a	47.82
Q9H813	TMEM206	Transmembrane protein 206	46.94
P30048	PRDX3	Thioredoxin-dependent peroxide reductase, mitochondrial	46.62
Q96KP4	CNDP2	Cytosolic non-specific dipeptidase	46.07
A0A087X072	RECQL4	ATP-dependent DNA helicase Q4	45.85
Q4G0X0	DMD	DMD protein	45.36
A0A0C4DGR2	PTOV1	Prostate tumor overexpressed gene 1. isoform CRA_d	45.05
P05062	ALDOB	Fructose-bisphosphate aldolase B	44.56
Q9Y6N5	SQRDL	Sulfide:quinone oxidoreductase. mitochondrial	44.15
K7EIL6	uncharacterized	Uncharacterized protein (Fragment)	43.8
K7ESL4	RAD51D	DNA repair protein RAD51 homolog 4	43.8
Q86XW9	NME9	Thioredoxin domain-containing protein 6	43.45
P54257	HAP1	Huntingtin-associated protein 1	42.61
Q16352	INA	Alpha-internexin	42.26

Q96T88	UHRF1	E3 ubiquitin-protein ligase UHRF1	42.07
Q8TDB8	SLC2A14	Solute carrier family 2. facilitated glucose transporter member 14	40.63
O94989	ARHGEF15	Rho guanine nucleotide exchange factor 15	40.44
A0A087X0B9	PTPRQ	Phosphatidylinositol phosphatase PTPRQ	39.86
A0A087WZU1	PTPRQ	Phosphatidylinositol phosphatase PTPRQ	39.86
Q96P48	ARAP1	Arf-GAP with Rho-GAP domain. ANK repeat and PH domain-containing protein 1	39.54
A1A4Y4	IRGM	Immunity-related GTPase family M protein	38.35
A0A087WTJ0	RECQL4	ATP-dependent DNA helicase Q4 (Fragment)	38.16
O43426	SYNJ1	Synaptojanin-1	37.8
Q14BN4	SLMAP	Sarcolemmal membrane-associated protein	37.58
P13489	RNH1	Ribonuclease inhibitor	36.97
Q4KMQ1	TPRN	Taperin	36.3
A0A0J9YYG8	DLG5	Disks large homolog 5 (Fragment)	35.03
Q9C0H5	ARHGAP39	Rho GTPase-activating protein 39	34.19
Q9P2E2	KIF17	Kinesin-like protein KIF17	33.08
Q01546	KRT76	Keratin. type II cytoskeletal 2 oral	32.85
O95936	EOMES	Eomesodermin homolog	32.42
Q86VW1	SLC22A16	Solute carrier family 22 member 16	32.27
H0Y3F1	SCNN1D	Amiloride-sensitive sodium channel subunit delta (Fragment	32.09
Q9UJV3	MID2	Probable E3 ubiquitin-protein ligase MID2	31.99
Q6ZMY3	SPOCD1	SPOC domain-containing protein 1	29.75
Q5XKE5	KRT79	Keratin, type II cytoskeletal 79	27.42
P12035	KRT3	Keratin, type II cytoskeletal 3	27.42
Q9UBT2	UBA2	SUMO-activating enzyme subunit 2	25.08
Q8NDM7	CFAP43	Cilia- and flagella-associated protein 43	20.5
Q99728	BARD1	BRCA1-associated RING domain protein 1	19.8
E9PPM7	SPOCD1	SPOC domain-containing protein 1	18.83
Q14693	LPIN1	Phosphatidate phosphatase LPIN1	18.83
H0Y390	MACF1	Microtubule-actin cross-linking factor 1. isoforms 1/2/3/5 (Fragment)	11.09

Identified proteins are organized according to the PLGS score. Identification is based on protein ID from UniProt protein database (http://www.uniprot.org/).